Vehicular Position Tracking Using LTE Signals

Marco Driusso, Chris Marshall, Mischa Sabathy, Fabian Knutti, Heinz Mathis, *Member, IEEE*, and Fulvio Babich, *Senior Member, IEEE*

***Abstract*—This paper proposes and validates, in the field, an approach for position tracking that is based on Long-Term Evolution (LTE) downlink signal measurements. A setup for real data live gathering is used to collect LTE signals while driving a car in the town of Rapperswil, Switzerland. The collected data are then processed to extract the received LTE cell-specific reference signals (CRSs), which are exploited for estimating pseudoranges. More precisely, the pseudoranges are evaluated by using the "ESPRIT and Kalman Filter for Time-of-Arrival Tracking" (EKAT) algorithm and by taking advantage of signal combining in the time, frequency, spatial, and cell ID domains. Finally, the pseudoranges are corrected for base station's clock bias and drift, which are previously estimated, and are used in a positioning filter. The obtained results demonstrate the feasibility of a position tracking system based on the reception of LTE downlink signals.**

***Index Terms*—Clock bias and drift estimation, ESPRIT, extended Kalman filter (EKF), Kalman filter (KF), Long-Term Evolution (LTE), positioning, range measurements, time-of-arrival (TOA) estimation.**

I. Introduction

NOWADAYS, navigation devices are commonly used in a large variety of contexts. These devices usually exploit a global navigation satellite system (GNSS) to accomplish the localization task. However, devices can often move from areas where GNSSs work effectively to environments where the sky view is limited, such as subterranean and indoor areas, narrow urban canyons, dense forests, etc. There, it may be impossible to obtain a position fix due to satellite reception being limited in angle and power. Addressing the problem of positioning in these environments is fundamental, and its application is not only limited to navigation but to other scenarios as well, such as asset management and the localization of emergency calls [1], [2].

Several methods have been proposed to tackle positioning in critical scenarios, e.g., inertial navigation systems, fingerprint-based positioning, and localization via wireless terrestrial signals. While the former have the disadvantage of cumulative errors and extensive calibration campaigns, respectively, the latter may provide good performance and coverage with the advantage of no additional infrastructure deployment [3]–[5]. In this context, localization by means of the cellular-system base-station (BS) downlink signals is a promising approach because of their wide availability and coverage, also bearing in mind the future deployments of micro-/picocells. Consequently, positioning using Third-Generation Partnership Project Long-Term Evolution (LTE) downlink signals has become a subject of recent research interest.

The LTE standard itself offers positioning capabilities, providing the positioning reference signal (PRS) and network-centered procedures for localizing the user equipment by exploiting PRS time-difference-of-arrival (TDOA) measurements [6], [7]. Several works, based on computer simulations [8], [9] or experimental evaluations [10]–[12], have been published on the subject of TDOA-based positioning systems that exploit LTE signals (either the PRS or other downlink signals) in harsh propagation environments. Recently, a few works recognized that newly deployed LTE commercial networks are not mature yet for TDOA-based positioning, mainly because of a lack of PRS transmission and because of nonsynchronized BSs [13]. The advancements in LTE positioning services are consequently limited by network operators' deployments. Fortunately, as pointed out in [13]–[16], other LTE downlink signals exist, which may be exploited opportunistically for positioning measurements, with no constraints on the BSs' clock synchronization. This enables LTE-based localization with limited operators' efforts in terms of additional infrastructure. However, to the best of the authors' knowledge, there are no studies in the literature that demonstrate an experimental real-world validation of such a concept.

Against this background, this paper proposes and validates in the field an approach for positioning by means of LTE downlink signals' time of arrival (TOA) measurements. The proposed system is mobile centered, it uses the signals transmitted by the currently deployed commercial LTE networks, and it relies on two assumptions. First, the BS positions have to be known to the receiver. Second, each BS has to make its clock properties available to the positioning engine (PE), which performs the location estimation, enabling a reasonably approximate knowledge of each BS's clock offset and drift in respect to a reference time. The PE might be internal within the network or located on the mobile receiver, and the clock properties of the BSs may be collected by appropriate location measurement units (LMUs). In the presented experiments, the BS positions were acquired from a public database, and the BSs' clock properties were estimated in a preliminary phase.

Manuscript accepted July 6, 2016.

M. Driusso is with u-blox Italia S.p.A., 34010 Sgonico, Italy (e-mail: marco.driusso@u-blox.com).

C. Marshall is with u-blox UK Ltd., Reigate RH2 9QQ, UK (e-mail: chris.marshall@u-blox.com).

M. Sabathy, F. Knutti, and H. Mathis are with the Institute for Communications Systems, Hochschule für Technik Rapperswil, 8640 Rapperswil, Switzerland (e-mail: mischa.sabathy@hsr.ch; fabian.knutti@hsr.ch; hmathis@hsr.ch).

F. Babich is with the Department of Engineering and Architecture, University of Trieste, 34127 Trieste, Italy (e-mail: babich@units.it).

With respect to the state of the art, the presented work demonstrates the feasibility of positioning by exploiting real LTE signals collected in the field from a commercial network and processed by means of a super-resolution algorithm (SRA)-based ranging technique. The experimental system adopts the "ESPRIT and Kalman filter for time of Arrival Tracking" (EKAT) ranging framework described in [17], which is able to effectively mitigate detrimental effects of multipath on LTE-based range estimations and the positioning algorithm of [16]. By using the software-defined radio (SDR) measurement setup of [16] and [17], the positioning system has been validated using the real LTE signals taken in a real environment from the commercial LTE network of the town of Rapperswil, Switzerland. Building on the work of Driusso *et al.* [17], where the transmitting LTE antenna ports were exploited for improving the measurement of the TOA, this work adds several contributions, particularly regarding the time–frequency combining of the LTE signals, the selection of range measurements from multiple cells pertaining to the same BS, and consideration on the effect of all these improvements on the estimation of the position. As a result, the pseudorange estimation performance is improved by exploiting the combination of the signals in the time, frequency, spatial, and cell ID domains.

The remainder of this paper is organized as follows. Section II explains the LTE downlink signals exploited for ranging. Section III describes the measurement setup. Sections IV and V show the employed TOA estimation algorithm and the combination method used for exploiting measurements from multiple BS cells. Section VI describes the estimation process of BSs' clock properties and how the TOA-based pseudoranges are corrected to obtain actual ranges. Section VII shows the adopted positioning algorithm. Finally, Section VIII comments on the obtained ranging and positioning results, followed by some final considerations in Section IX.

Notation: Matrices and vectors are denoted as uppercase and lowercase boldface letters, respectively, e.g., $\mathbf{A} \in \mathbb{C}^{M\times N}$ and $\boldsymbol{a} \in \mathbb{C}^{M}$. $\hat{a}, \hat{\boldsymbol{a}}$ and $\hat{\mathbf{A}}$ denote the estimates of $a, \boldsymbol{a}$ and $\mathbf{A}$, respectively. $\mathbf{I}_P$ is the $P \times P$ eye matrix, $\mathbf{0}_{P\times Q}$ is an $P \times Q$ all-zero matrix, and $\mathbf{0}_P$ is a length P all-zero vector. The operators $(\cdot)^T$, $(\cdot)^H$, $(\cdot)^{-1}$, and $(\cdot)^\dagger$ denote the transpose, the Hermitian transpose, the inverse, and the Moore–Penrose pseudoinverse of a matrix, respectively. $\langle\cdot\rangle_x$ is the modulo x operation. $\mathcal{F}\{\cdot\}$, DFT$\{\cdot\}$, and IDFT$\{\cdot\}$ denote, respectively, the direct continuous time, direct discrete, and inverse discrete Fourier transforms, respectively. $\mathbb{E}[\cdot]$ is the expected value of a random variable (RV). $|\cdot|$ and $\arg\{\cdot\}$ are the absolute value and the argument of a complex number, respectively. $c \simeq 299\,792\,458$ m/s is the speed of light. $\|\cdot\|$ denotes the norm of a vector. The index t is generally employed as a discrete time index identifying the tth performed measurement, with $t^{(U)}$ being the corresponding coordinated universal time (UTC) epoch.

II. Long-Term Evolution Signals Used for Ranging

Here, the characteristics of the exploited LTE downlink signals are briefly described. Moreover, details on the particular LTE parameters found during the measurements in Rapperswil are given. This does not limit the generality of the obtained results. More complete information about the LTE physical layer can be found in the specifications [6].

TABLE I
LTE Physical-Layer Parameters Found in Rapperswil

parameter	operator 1	operator 2
B	15 MHz	10 MHz
$N_{\mathrm{RB}}^{\mathrm{DL}}$	75	50
$N_{\mathrm{sc}} = N_{\mathrm{sc}}^{\mathrm{RB}}\, N_{\mathrm{RB}}^{\mathrm{DL}}$	900	600
carrier frequency f_{C}	1815.1 MHz	1869 MHz
N_{fft}	1024	
$\Delta f = 1/T_{\mathrm{s}}$	15 KHz	
$N_{\mathrm{sc}}^{\mathrm{RB}}$	12	
$N_{\mathrm{symb}}^{\mathrm{DL}}$	7	
base time unit $T_{\mathrm{s},0}$	$T_{\mathrm{s}}/2048$	
$l = 0$ CP length $T_{\mathrm{CP},0}$	$160{\cdot}T_{\mathrm{s},0}$	
$l > 0$ CP length $T_{\mathrm{CP},l}$	$144{\cdot}T_{\mathrm{s},0}$	

The downlink physical layer of the LTE standard for the frequency-domain duplexing (FDD) scheme is organized in 10 ms long radio frames, each made of ten subframes, which contain two slots (20 slots per radio frame, 0.5 ms per slot). Each slot contains $N_{\mathrm{symb}}^{\mathrm{DL}}$ orthogonal frequency division multiplexing (OFDM) symbols, each carrying $N_{\mathrm{sc}} = N_{\mathrm{RB}}^{\mathrm{DL}} N_{\mathrm{sc}}^{\mathrm{RB}}$ subcarriers. The parameter $N_{\mathrm{RB}}^{\mathrm{DL}}$, which ultimately determines the number N_{sc} of subcarriers per each OFDM symbol, is related to the cell channel bandwidth B. The same LTE BS can transmit on multiple cells, usually spatially multiplexed by means of directional antennas. In the following, LTE cells will be identified either by their cell ID $N_{\mathrm{ID}}^{\mathrm{cell}}$ or, for notational simplicity, by an index $i \in \mathbb{N}$. On each cell, the BS may transmit using multiple antennas, referred to as antenna ports, and identified by the index p. Finally, it is worth mentioning that LTE is designed to operate with a frequency reuse factor of one, meaning that neighbor cells can transmit on the same channel, enabling simultaneous nonorthogonal reception of multiple cells.

At the time of measurements[1] the LTE network of Rapperswil was found to be using FDD and to use a normal OFDM cyclic prefix (CP) and a two-antenna-port configuration, meaning that each BS was set up to transmit from two antennas, identified by $p = \{0, 1\}$. Table I summarizes all the other useful LTE parameters found during the measurements, in which signals from two LTE operators were detected.

Each LTE signal can be defined using a time–frequency grid for each antenna port p, where each element of the grid $S_l^p[k]$, referred to as a resource element (RE), corresponds to a particular subcarrier k in the OFDM symbol l of a slot. The actual baseband analog signal is obtained with a classical OFDM modulation with empty dc subcarrier, as [6]

$$s_l^p(t) = \sum_{k=-N_{\mathrm{sc}}/2}^{k=-1} S_l^p[k + N_{\mathrm{sc}}/2] e^{j2\pi k\Delta f t} + \sum_{k=0}^{k=N_{\mathrm{sc}}/2-1} S_l^p[k + N_{\mathrm{sc}}/2] e^{j2\pi(k+1)\Delta f t},\ t \in [-T_{\mathrm{CP},l}, T_s] \tag{1}$$

[1]The data set used for the results reported in the paper was acquired on August 28, 2014.

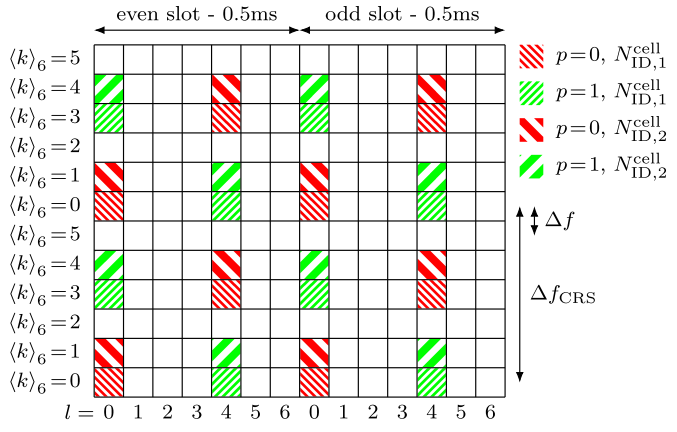

Fig. 1. Mapping to REs of the CRS for $p = 0$ and $p = 1$ of two different cell IDs. The indexes k and l identify subcarriers (i.e., FD) and OFDM symbols (i.e., time domain), respectively.

where $T_{\mathrm{CP},l}$ is the duration of the lth symbol CP, $T_s = 1/\Delta f$ is the duration of the actual OFDM symbol, $l = 0, \ldots, N_{\mathrm{symb}}^{\mathrm{DL}} - 1$, and t denotes here the continuous-time variable. Usually, for reducing the implementation complexity, (1) is generated as a digital-to-analog conversion of a CP extended version of $s_l^p[n] = \mathrm{IDFT}\{S_l^p[k]\}$,[2] with an IDFT operator of length N_{fft}.

For the range measurements described in this paper, the cell-specific reference signal (CRS) was exploited. This is a downlink reference signal intended for channel estimation for coherent data demodulation and is particularly suitable for our purposes since it fully occupies the available bandwidth and, differently to the PRS, its transmission is mandatory. The CRS consists of a quadrature phase-shift keying (QPSK)-modulated Gold sequence mapped to the REs as shown in the grid of Fig. 1, where only two slots and $N_{\mathrm{sc}}^{\mathrm{RB}} = 12$ subcarriers are represented. The complete frequency domain (FD) mapping of the CRS can be obtained by repeating the grid $N_{\mathrm{RB}}^{\mathrm{DL}}$ times vertically. A BS transmits a particular CRS for each cell it owns, and each antenna port of the cell, with a mapping to REs that depends on both $N_{\mathrm{ID}}^{\mathrm{cell}}$ and p. When using two antenna ports, a CRS transmission occurs twice per slot, in OFDM symbols $l = 0$ and $l = 4$: for each $l \in \{0, 4\}$, a different CRS is transmitted from each antenna port in the same OFDM symbol in nonoverlapping subcarriers, as Fig. 1 depicts. Since the CRS pilot tones occupy one subcarrier every six through all the available bandwidth (with a spacing of $\Delta f_{\mathrm{CRS}} = 6\Delta f$), the total number of transmitted pilot tones is $N_{\mathrm{tot}} = N_{\mathrm{sc}}/6$ per antenna port per OFDM symbol. As shown in Fig. 1, CRSs pertaining to different cell IDs differ for an FD shift, enabling orthogonal CRS transmission from the cells controlled by the same BS.

III. Measurements in Real Conditions

A. Measurement Setup

The proposed approach has been tested with a live data set of commercial LTE signals recorded in Rapperswil. The setup

[2]Without loss of generality, the DFT and IDFT operations may be easily defined to realize exactly the modulation of (1), guaranteeing the empty dc subcarrier.

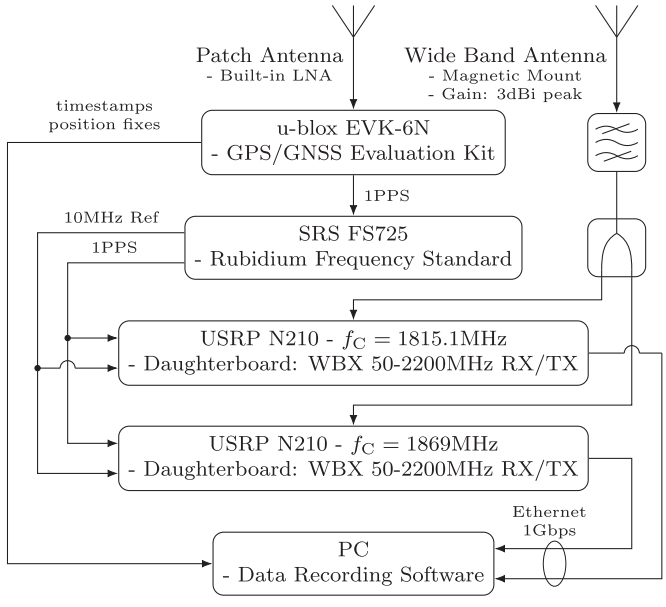

Fig. 2. Flow graph of the portable measurement setup.

used to gather the live data is shown in Fig. 2 and consists of two Universal Software Radio Peripheral (USRP) N210 SDRs, driven by a high-precision 10 MHz reference clock from a GPS-locked Rubidium frequency standard. One USRP was used for each operator to cover the different downlink carrier frequencies f_C. A conventional personal computer was used as a system controller and for data storage. The recorded data were GPS timestamped; therefore, coherent known sampling of the two USRPs was guaranteed, allowing the LTE signals of the two different operators to be used in combination. Sampling at a rate of 25 megasamples per second generates 100 MB of data per second and per operator. To reduce this amount, only 10 ms chunks of contiguous data were stored every second. The data recording equipment was installed on a trolley, and energy was supplied by a battery-powered dc-to-ac converter, allowing field usage. The LTE signal data was gathered in the area of Rapperswil with the equipment installed in a van. The route was chosen such as to include urban, suburban, and open-field areas, as the GPS track in Fig. 3 suggests. This routing allows the performance of the proposed system to be analyzed in different propagation environments. The time needed for driving the route shown was about 20 min at speeds up to 50 km/h. When available, the GPS fix corresponding to the reception position of each recorded chunk was saved, to be used as a ground truth. The complete GPS track has been visually inspected and superimposed on a map, and the correspondence between the GPS estimations and the actual path traveled by the van has been verified. Except for a few rare cases, the GPS track was always within the width of the actual street lane on which the receiver was located, indicating a tolerance for the GPS track of a maximum of roughly 4 m.

B. Cell Search and Coarse Synchronization

The first task in analyzing the recoded data is to find and extract the LTE signals that have been received. The recorded

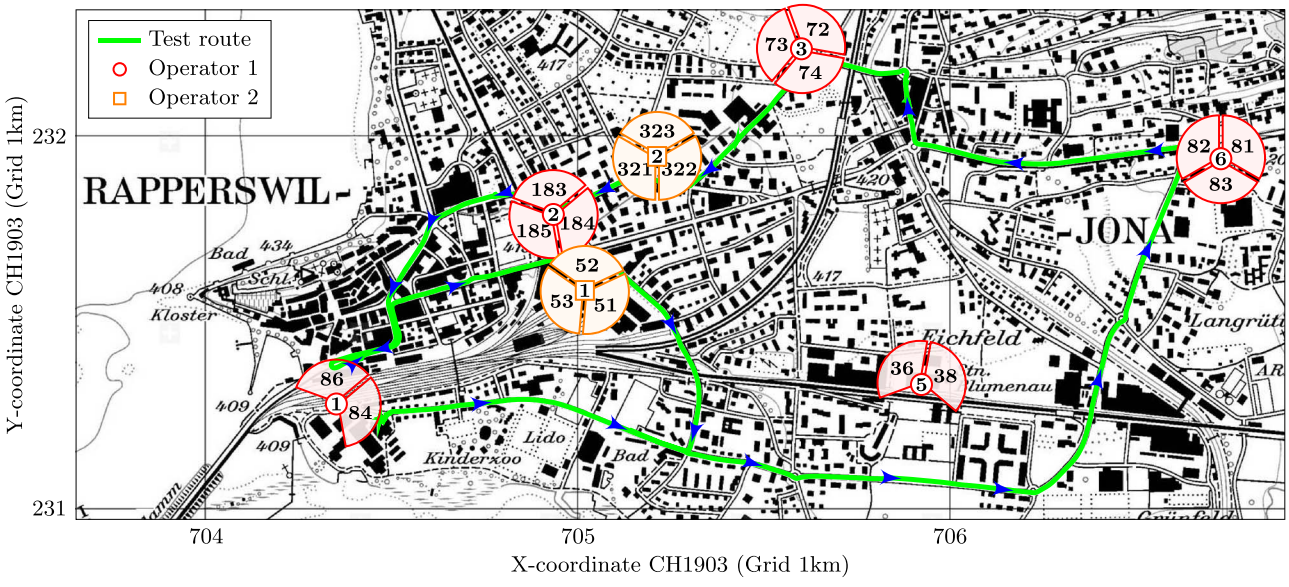

Fig. 3. Test route and detected LTE cells. Each indexed marker corresponds to a BS, which transmits on several cells, having the indicated $N_{\mathrm{ID}}^{\mathrm{cell}}$. The orientation of the cells is approximate. The cells of a third BS pertaining to operator 2 ($N_{\mathrm{ID}}^{\mathrm{cell}} = 460$ and $N_{\mathrm{ID}}^{\mathrm{cell}} = 461$), located south across the lake, were also detected and used for positioning.

data set was searched for signals from available BSs by means of an exhaustive search against a list of cell identities of all BSs in the area. Since the BS locations were assumed known, the location information provided by the Swiss Federal Office of Communications (OFCOM) was used [18]. After discovering all available BSs including their frame and symbol timing, the 10-ms chunks, which contain the signal of a certain BS, were marked per BS. From every chunk of raw data, for every BS received in that chunk, and every cell pertaining to each BS, a particular slot in the frame was selected, on the basis of the received SNR.

Then, the two OFDM symbols containing the CRS in the selected slot were saved for further processing, together with the UTC timestamp $t^{(U)}$ of the chunk reception, and the offset Δt_s^i introduced in respect to $t^{(U)}$ for synchronizing on the symbol timing of cell i.

The recorded data set contained signals from a total of nine BSs, with six BSs from operator 1 and three BSs from operator 2. Fig. 3 shows the locations of the BSs used, except for a distant BS across the lake in south–southeast direction (BS 3, operator 2) and another BS situated on a hill to the north (BS 4, operator 1, not considered for positioning). All BSs were found to be using a two-antenna-port configuration.

IV. Estimating Time-of-Arrival-Based Pseudoranges

The TOA of the LTE signals can now be estimated, ready for use for position estimation as described in the later Section VII. As explained in Section II, the TOA of the LTE CRS is used to measure a pseudorange from each received BS. These measurements are affected by the multipath experienced by the signal as a result of the propagation channel.

In a short observation window, the multipath channel encountered by a signal propagating from a BS to a mobile receiver may be modeled with the following channel impulse response (CIR) and channel frequency response (CFR) [19]

$$h(\tau) = \sum_{l=0}^{L-1} h_l \delta(\tau - \tau_l) \overset{\mathcal{F}\{\cdot\}}{\Rightarrow} H(f) = \sum_{l=0}^{L-1} h_l e^{-j2\pi f \tau_l}. \quad (2)$$

In (2), $\delta(\cdot)$ denotes the Dirac delta function, $h_l \in \mathbb{C}$ is the complex channel gain associated to the lth path, and τ_l is the corresponding delay, with $\tau_0 < \cdots < \tau_{L-1}$. Due to the OFDM modulation that underlies their physical layer, LTE downlink signals offer a very convenient way of estimating the CFR by exploiting the CRS pilot tones. This CFR estimation constitutes a convenient basis for the direct path (DP) TOA estimation and is evaluated with the following procedure.

Let $r_{t,l}^i[n], n = 0, \ldots, N_{\mathrm{fft}} - 1$, be the result of the analog-to-digital conversion of the lth OFDM symbol (after CP removal) received in the slot measured at time t from cell i. The index l can assume here the values $l = 0$ or $l = 4$ as only the two OFDM symbols of a slot carrying the CRS have been extracted from the signal data. The content of the subcarriers in the received signal can be easily accessed with conventional OFDM demodulation techniques as $R_{t,l}^i[k] = \mathrm{DFT}\{r_{t,l}^i[n]\}$. Then, a simple least squares (LS) CFR estimation for each transmit antenna port is possible due to the knowledge of the corresponding CRS pilot tones $S_l^p[k]$, e.g., as described in [20]. Hence, for each antenna port $p = \{0, 1\}$ and OFDM symbol $l = \{0, 4\}$, the CFR LS estimation $\hat{H}_{t,l}^{i,p}[k], k = 0, \ldots, N_{\mathrm{tot}} - 1$ can be calculated, where each sample in $\hat{H}_{t,l}^{i,p}[k]$ is displaced of $6\Delta f$, as a consequence of the CRS pilot FD spacing. This procedure leads to a total of four CFR LS estimates for every measurement index t, one per antenna port $p = \{0, 1\}$ for each OFDM symbol $l = \{0, 4\}$ carrying CRS. These CFR estimations are used in the presented framework for estimating the DP TOA τ_0.

The use of the CFR for the TOA estimation is particularly useful because it permits a convenient integration of the proposed

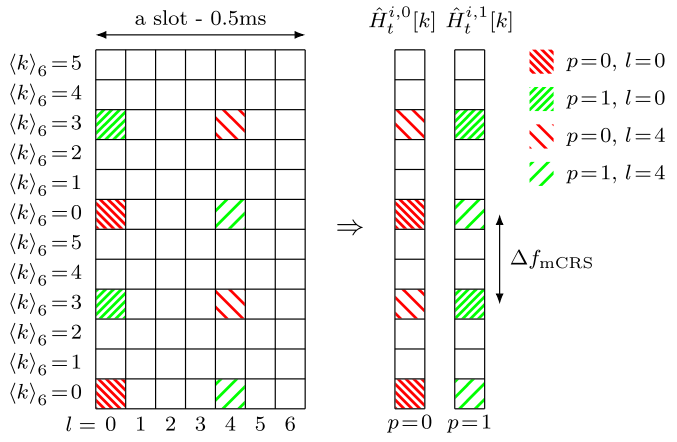

Fig. 4. Example of merging the CFR LS estimates $\hat{H}_{t,l}^{i,p}[k]$ evaluated using the two CRSs of a slot, for each antenna port.

positioning approach into LTE communication modules since the CFR estimation is commonly already performed by LTE receivers for coherent demodulation of the user data [21].

A. Time–Frequency Combination of Multiple CFR Estimates

The sets of CFR LS estimates obtained using the CRS pilot tones can now be combined with the aim of improving the TOA estimation performance. According to the mapping shown in Fig. 1, the subcarriers of the two CRSs of a slot are characterized by a relative FD shift of $3\Delta f$. Due to the fairly low speeds involved in the considered test case, which determined a sufficient time correlation of the channel's phase and magnitude, this aspect of the CRS design may be exploited by merging the two estimates $\hat{H}_{t,0}^{i,p}[k]$ and $\hat{H}_{t,4}^{i,p}[k]$, as shown in Fig. 4. This time–frequency combination permits to obtain the length $2N_{\mathrm{tot}}$ CFR estimate $\hat{H}_t^{i,p}[k]$, which is characterized by a frequency separation of $\Delta f_{\mathrm{mCRS}} = 3\Delta f$ between samples. Depending on the TOA estimation algorithm adopted, the increased number of samples for each CFR estimate $\hat{H}_t^{i,p}[k]$ and the smaller frequency separation $\Delta f_{\mathrm{mCRS}} < \Delta f_{\mathrm{CRS}}$ may correspond to increased resolution and increased maximum TOA computable, respectively.

Five algorithms have been used in this paper to estimate the DP TOA out of the channel estimates $\hat{H}_t^{i,p}[k]$, each characterized by different timing error performance and complexity. In particular, four CIR-based TOA estimators are presented in Section IV-B, whereas a more complex but robust TOA estimator is described Section IV-C.

B. CIR-Based TOA Estimation Algorithms

The starting point for practical TOA estimators is to use the CFR estimation $\hat{H}_t^{i,p}[k]$, $k = 0, \ldots, 2N_{\mathrm{tot}} - 1$, to compute the corresponding discrete CIR as

$$\hat{h}_t^{i,p}[n] = \mathrm{IDFT}\left\{\hat{H}_t^{i,p}[k]\right\},\ n = 0, \ldots, 2N_{\mathrm{tot}} - 1. \qquad (3)$$

This CIR spans the time interval $[-1/(2\Delta f_{\mathrm{mCRS}}), 1/(2\Delta f_{\mathrm{mCRS}})] = [-11.11\ \mu\mathrm{s}, 11.11\ \mu\mathrm{s}]$, and can be exploited for realizing practical TOA estimation algorithms.

The simplest approach may be the one of [22], where the TOA is obtained with a parabolic interpolation around the maximum of $|\hat{h}_t^{i,p}[n]|$. Throughout this paper, this method is referred to as IDFT-MAX (IM). Although attractive for its computational simplicity, the IM method is not robust against multipath because harsh propagation environments are typically characterized by a DP that is not necessarily the strongest path. A simple countermeasure may be the adoption of a non-line-of-sight (NLOS) rejection mechanism, such as that in [16]. This comprises the evaluation of the N_{IL} highest CIR peaks, where N_{IL} is a parameter subject to empirical tuning. Then, the measure is considered a line-of-sight (LOS) case only if the maximum of the CIR is the earliest peak between the N_{IL}, in which case it is passed on for use in the PE. Conversely, if one of the N_{IL} peaks appears before the CIR maximum, the measurement is labeled as a NLOS case, and is discarded and not used in the PE. This method is referred to as IDFT-LOS (IL). It is quite robust in identifying NLOS measurements, but it has the drawback of discarding NLOS cases without producing TOA estimates, resulting in a smaller number of available pseudoranges, and ultimately in reduced accuracy and reduced positioning yield. As an example, in the case of three BSs visible, with two in LOS and one in NLOS conditions, IL will pass to the PE only two pseudoranges, resulting in reduced positioning accuracy. IM and IL have been considered since they are estimators that can be realized on an LTE communication module with limited additional processing cost since the CIR computation is usually performed already for communication purposes.

Two other practical TOA estimators have been considered, which are based on the assumption that the estimated CIR is made up of the sum combination of a signal component and of a complex Gaussian noise component. As a consequence, the samples of the power delay profile (PDP) $\hat{p}_t^{i,p}[n] = |\hat{h}_t^{i,p}[n]|^2$ can be considered RVs having a χ^2 distribution. Based on this assumption, the "TOA estimation based on model order selection" (TEMOS) estimator of [23] and the threshold-to-noise ratio (TNR)-based estimator of [24] have been used in the presented experiments. The TEMOS algorithms use the theory of model order selection to find the most likely partitioning of the samples of $\hat{p}_t^{i,p}[n]$ into samples comprising just noise and samples containing signal and noise. TEMOS then assumes the DP TOA estimate to be the first sample in the signal plus noise subset [23]. Throughout this paper, this method is referred to as TE. Differently, the TNR-based estimator sets a threshold according to an estimated noise variance and to a TNR that determines a target early probability detection [24]. This method is referred to as TN. For exploiting the multiple signals available due to the transmission of multiple antenna ports, the combined PDP $\hat{p}_t^{i}[n] = (1/2)(\hat{p}_t^{i,0}[n] + \hat{p}_t^{i,1}[n])$ has been considered the input of the TE and TN estimators. Moreover, the TE and TN estimators are originally intended for ultrawide bandwidth signals; hence, proper windowing is required on the PDP for reducing the biasing effect of sidelobes. Compared with the previous IM and IL estimators, these χ^2-statistic-based estimators can deal with NLOS conditions.

In Fig. 5, an example of the results given by the CIR-based TOA estimators described earlier is given, using the signals received from the two antenna ports of cell $N_{\mathrm{ID}}^{\mathrm{cell}} = 51$, BS 1,

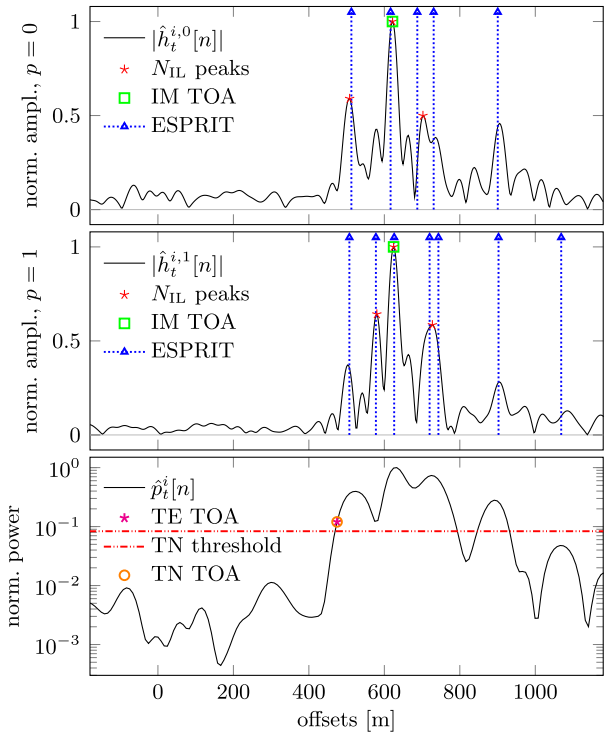

Fig. 5. Example of the results given by the IM, IL, TE, and TN TOA estimators using the signals received from the two antenna ports of cell $N_{\mathrm{ID}}^{\mathrm{cell}} = 51$, BS 1, and operator 2 at $t = 2561$. All time estimates are expressed in respect to the UTC epoch $t^{(U)} + \Delta t_s^i$ and shown as distance offsets.

operator 2 at $t = 2561$. The two upper plots show the CIRs corresponding to the two antenna ports, and the corresponding IM and IL TOA estimates. The ESPRIT multipath TOA estimates are also shown as a more accurate reference, computed as described later in Section IV-C1. As one can note, the CIRs pertaining to different antenna ports exhibit different multipath but similar DP TOA. The IM estimations fails to locate what appears to be the DP (i.e., the path at offset around 500 m), whereas the IL estimator correctly recognizes the measurement as a NLOS case, and discards it. The bottom plot also shows the PDP $\hat{p}_t^i[n]$ together with the TE and TN TOA estimates. This illustrates how TE and TN produce a TOA estimate which is on a rising edge of the PDP, instead of on a PDP peak; hence, a proper constant offset correction Δt_o is needed, which depends on the adopted windowing technique. Moreover, the widening effect of windowing on the lobes of the PDP is visible.

C. EKAT Algorithm

In addition to the DP TOA estimation algorithms directly based on the CIR considered in Section IV-B, an estimator which is more robust against multipath is considered, at the cost of an increase in the complexity. More particularly, the EKAT ranging algorithm is employed. This algorithm has been developed mainly for assessing the feasibility of ranging with realistic LTE signals, for studying the influence of multipath on the achieved ranging performance, and for obtaining a reference best case performance for future developments of multipath-robust practical TOA estimators, suitable for real-time implementation. The algorithm was partially described in [17], and its working principles will be reported here with more details.

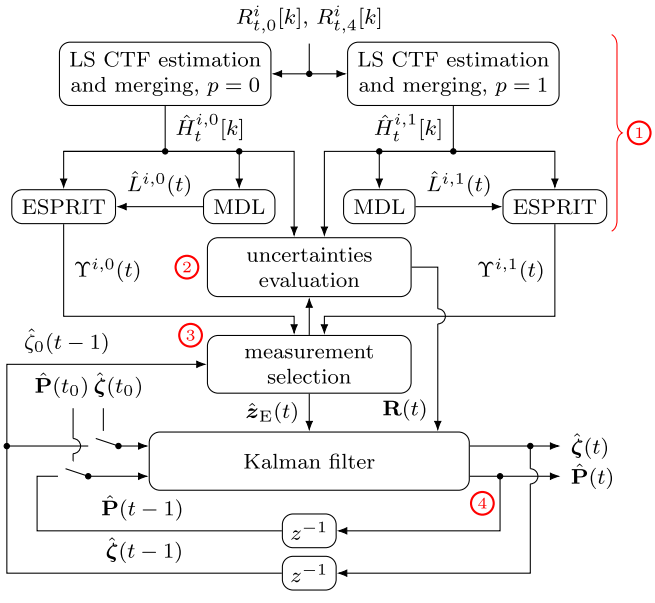

Fig. 6. Flow graph of the EKAT algorithm applied to the signals measured from the cell i. The numbering in the red markers correspond to the paragraphs within Section IV-C.

Briefly, the EKAT algorithm consists of the following steps. First, the multipath is separated by means of a SRA, as described in Section IV-C1, and the uncertainties corresponding to the estimated multipath TOA are evaluated using a bound-based approach, reported in Section IV-C2. Then, the DP is selected from the estimated set of multipath TOA with the heuristic approach of Section IV-C3, and passed, together with the corresponding uncertainty, to a conventional Kalman filter (KF). Finally, the KF tracks the DP by exploiting the received measurements and the model discussed in Section IV-C4. The flow graph of the EKAT algorithm is shown in Fig. 6, with the numbered blocks described in the following.

1) TOA Estimation With Super-Resolution Algorithms: SRAs are a well-known approach for multipath TOA estimation, e.g., documented in [25]–[27] and the references therein, which exploit the fact that a multipath channel frequency response is modeled as a harmonic model, i.e., as a sum of complex sinusoids. The EKAT algorithm exploits the minimum description length (MDL) criterion for the estimation of the number of received multipath components L, and the ESPRIT SRA for the estimation of the multipath delays $\tau_l \; \forall \, l$. In the presented experiments, this estimation is performed for each detected cell i, measurement instant t, and antenna port p, by exploiting each CFR estimate $\hat{H}_t^{i,p}[k]$, $k = 0, \ldots, 2N_{\mathrm{tot}} - 1$, computed as in Section IV-A, as follows.

The samples of $\hat{H}_t^{i,p}[k]$ are arranged in length M snapshots $\boldsymbol{x}_t^{i,p}[k]$, which are used to build the so-called data matrix $\mathbf{X}_t^{i,p}$, i.e.,

$$\mathbf{X}_t^{i,p} = \frac{1}{\sqrt{N}} \left[\boldsymbol{x}_t^{i,p}[0], \ldots, \boldsymbol{x}_t^{i,p}[N-1] \right] \in \mathbb{C}^{M \times N} \quad (4)$$

$$\boldsymbol{x}_t^{i,p}[k] = \left[\hat{H}_t^{i,p}[k], \ldots, \hat{H}_t^{i,p}[k+M-1] \right]^T \in \mathbb{C}^M \quad (5)$$

where $N = 2N_{\text{tot}} - M + 1$ is the number of snapshots used, and M is a design parameter of the SRA. M is usually chosen as $M = \bar{m}2N_{\text{tot}}$, with $\bar{m} \in]0, 1[$ being a parameter subject to empirical tuning. A value of $\bar{m}$ closer to the unity ensures increased resolution in multipath separation, at the cost of decreased averaging of noise [26]. In this paper, $\bar{m}$ has been determined with a set of experiments on a preliminary continuous LTE signal data set, to minimize the variance of the estimated multipath TOA.

A singular value decomposition of the data matrix[3] $\mathbf{X}$ is computed as $\mathbf{X} = \mathbf{U} \cdot \mathbf{\Sigma} \cdot \mathbf{V}^H$, with the matrices $\mathbf{U} \in \mathbb{C}^{M \times M}$ and $\mathbf{V} \in \mathbb{C}^{N \times N}$ being unitary, and $\mathbf{\Sigma} \in \mathbb{C}^{M \times N}$ being a diagonal matrix with the singular values $\sigma_1 \geq \cdots \geq \sigma_M$ in the main diagonal. This permits the evaluation of the parameters $(\sigma_m)^2$, $m = 1, \ldots, M$, which are the eigenvalues of the autocorrelation matrix $\hat{\mathbf{R}}_{\boldsymbol{x}} = \mathbf{X} \cdot \mathbf{X}^H \in \mathbb{C}^{M \times M}$, and are used in the MDL criterion for the estimation of the number $\hat{L}$ of multipath components in the considered CFR, as in [25] and [26]. Then, a classical ESPRIT approach is used for the estimation of the multipath delays, based on the following matrix manipulations [28]

$$\mathbf{U}_s = \mathbf{U} \cdot \left[\mathbf{I}_{\hat{L}} \mathbf{0}_{\hat{L} \times (M - \hat{L})}\right]^T \in \mathbb{C}^{M \times \hat{L}} \tag{6a}$$

$$\mathbf{U}_{s,1} = [\mathbf{I}_{M-1} \mathbf{0}_{M-1}] \cdot \mathbf{U}_s \in \mathbb{C}^{M-1 \times \hat{L}} \tag{6b}$$

$$\mathbf{U}_{s,2} = [\mathbf{0}_{M-1} \mathbf{I}_{M-1}] \cdot \mathbf{U}_s \in \mathbb{C}^{M-1 \times \hat{L}} \tag{6c}$$

$$\mathbf{\Psi} = \mathbf{U}_{s,1}^{\dagger} \cdot \mathbf{U}_{s,2} \in \mathbb{C}^{\hat{L} \times \hat{L}}. \tag{6d}$$

Finally, the $\hat{L}$ eigenvalues $\psi_0, \ldots, \psi_{\hat{L}-1}$ of $\mathbf{\Psi}$ are computed and then used to evaluate the multipath TOA as follows

$$\hat{\tau}_l = -\frac{1}{2\pi \Delta f_{\text{mCRS}}} \arg\{\psi_l\}, \; l = 0, \ldots, \hat{L} - 1. \tag{7}$$

From the fact that $\arg\{\psi_l\} \in [-\pi, \pi]$, $\forall\, l$, it follows that ESPRIT is capable of estimating a TOA in the interval $[-1/(2\Delta f_{\text{mCRS}}), 1/(2\Delta f_{\text{mCRS}})] = [-11.11\,\mu\text{s}, 11.11\,\mu\text{s}]$ around the instant of measure t.

As a result of the whole procedure described earlier, a set of $\hat{L}^{i,p}(t)$ multipath TOA $\Upsilon^{i,p}(t) = \{\hat{\tau}_0^{i,p}(t) < \cdots < \hat{\tau}_{\hat{L}^{i,p}(t)-1}\}$ is produced using the CFR estimation $\hat{H}_t^{i,p}[k]$ corresponding to the antenna port p of the ith sector at each measurement time t. It has to be noted that a well-known shortcoming of the MDL criterion is that it tends to overestimate L in case of large snapshot lengths M and high SNR values [29]–[31]. Hence, overestimated values of L may cause ESPRIT to produce TOA outliers, which may be even smaller than the actual DP TOA. EKAT overcomes this weakness using the measurement selection strategy described in Section IV-C3.

An example of the results obtained with the described multipath TOA estimation procedure is shown in the two plots of Fig. 7. There, for each measurement index t, up to the first four paths estimated using the CRSs of cell $N_{\text{ID}}^{\text{cell}} = 52$ operator 2 are shown for each antenna port. All the values are

[3]In the remainder of this section, the indexes i, t, p will be omitted for notational simplicity.

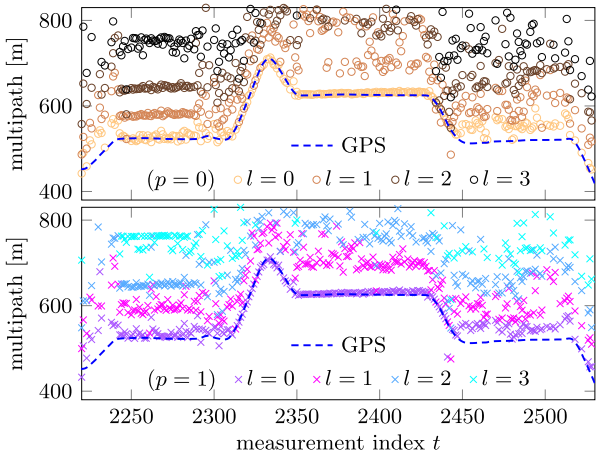

Fig. 7. Results of the ESPRIT TOA estimation from antenna ports $p = 0$ and $p = 1$ using the CRSs of cell $N_{\text{ID}}^{\text{cell}} = 52$ operator 2 in a representative time interval. All the estimated values are represented as actual ranges since already corrected for bias and drift. The GPS ground truth is also shown.

expressed as actual ranges and have been obtained by applying the offset correction described in Section VI to the pseudorange as $c \cdot (\hat{\tau}_l^{i,p}(t) + \Delta t_s^i)$, where Δt_s^i is the time offset introduced in respect to t for cell i symbol timing. As one can see, the first detected path has almost the same TOA for the two antenna ports, whereas the other paths are different.

2) Measurement Uncertainty Evaluation: EKAT evaluates the uncertainty associated with each estimated multipath TOA with the approach of [32], where it is demonstrated that the error affecting each ESPRIT outcome is a Gaussian RV with a variance that can be expressed in closed form.[4] More particularly, the ESPRIT error variance is expressed in [32] as a function of the true number of incoming waves and of the singular vectors and singular values of the exact data matrix $\tilde{\mathbf{X}}$, which is built in the same way as (4) and (5), except that the exact data values are used instead of the noisy ones. However, this approach is not feasible for real scenarios since the exact data and the actual number of incoming multipath components is unknown. Hence, EKAT relies on the use of the noisy data matrix $\mathbf{X}$ and of the estimated value $\hat{L}$. More particularly, to estimate the variance $\text{Var}(\epsilon_l)$ of the measurement error $\epsilon_l = \tau_l - \hat{\tau}_l$ relative to the lth TOA estimated with the ESPRIT, consider, in addition to the matrices (6a)–(6d), the following matrix decompositions of $\mathbf{U}$ and $\mathbf{\Sigma}$

$$\mathbf{U}_o = \mathbf{U} \cdot \left[\mathbf{0}_{(M-\hat{L}) \times \hat{L}} \mathbf{I}_{M-\hat{L}}\right]^T \in \mathbb{C}^{M \times (M-\hat{L})} \tag{8a}$$

$$\mathbf{U}_{o,1} = [\mathbf{I}_{M-1} \mathbf{0}_{M-1}] \cdot \mathbf{U}_o \in \mathbb{C}^{(M-1) \times (M-\hat{L})} \tag{8b}$$

$$\mathbf{U}_{o,2} = [\mathbf{0}_{M-1} \mathbf{I}_{M-1}] \cdot \mathbf{U}_o \in \mathbb{C}^{(M-1) \times (M-\hat{L})} \tag{8c}$$

$$\mathbf{\Sigma} = \begin{bmatrix} \mathbf{\Sigma}_{\hat{L}} & * \\ * & * \end{bmatrix}, \; \mathbf{\Sigma}_{\hat{L}} \in \mathbb{C}^{\hat{L} \times \hat{L}}. \tag{8d}$$

[4]In [32], the error of the ESPRIT algorithm is characterized when used for angle-of-arrival estimation of planar waves on linear antenna arrays. The same procedure in [32] was applied in this paper, with the changes needed to be used in the TOA estimation case.

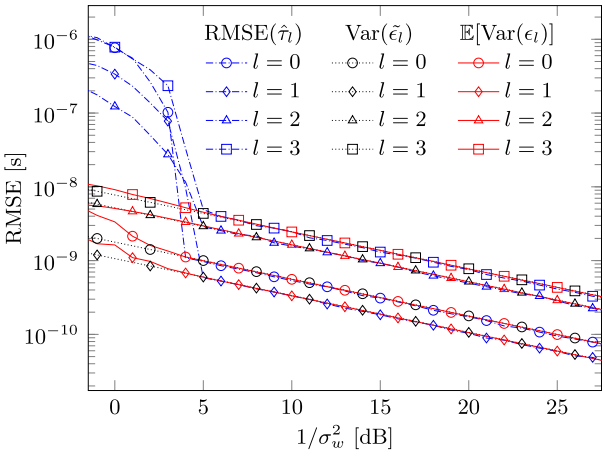

Fig. 8. Comparison between the average value of $\mathrm{Var}(\epsilon_l)$ (red solid lines) and $\mathrm{Var}(\tilde{\epsilon}_l)$ (black dotted lines). The RMSE of an ESPRIT estimation (blue dash-dotted lines) is also shown as a reference.

Then, the error variance relative to the lth ESPRIT estimate can be expressed exploiting the results of the study in [32] as

$$\mathrm{Var}(\epsilon_l) = \frac{C_l^2 \hat{\sigma}_w^2}{2} \left\| \boldsymbol{v}_l \mathbf{U}_{s,1}^{\dagger} (\mathbf{U}_{o,2} - \psi_l \mathbf{U}_{o,1}) \right\|^2 \left\| \boldsymbol{\Sigma}_{\hat{L}}^{-1} \boldsymbol{u}_l \right\|^2 \quad (9)$$

where $\hat{\sigma}_w^2$ is an estimate of the variance of the noise affecting the CFR samples $\hat{H}[k]$ and $\boldsymbol{u}_l, \boldsymbol{v}_l, \psi_l$ are respectively the lth left eigenvector, right eigenvector, and eigenvalue of $\boldsymbol{\Psi}$. Following the procedure of [32], it can be easily demonstrated that $C_l = -1/(2\pi \Delta f_{\mathrm{mCRS}})\ \forall l$. In the proposed algorithm, $\hat{\sigma}_w^2$ is obtained using the approach of [33], by exploiting the $M - \hat{L}$ smaller eigenvalues of $\hat{\mathbf{R}}_{\boldsymbol{x}}$, as

$$\hat{\sigma}_w^2 = \frac{1}{M - \hat{L}} \sum_{m=\hat{L}+1}^{M} (\sigma_m)^2. \quad (10)$$

The error variances $\mathrm{Var}(\epsilon_l)$ are evaluated using (9) for each ESPRIT multipath TOA estimation $\hat{\tau}_l^{i,p}(t) \in \Upsilon^{i,p}(t)$ obtained from antenna port p, sector i, at time t.

Monte Carlo simulations were performed to assess the effectiveness of this approach. The simulations showed a substantial agreement between the values of error variance calculated using the exact data matrix $\tilde{\mathbf{X}}$, denoted with $\mathrm{Var}(\tilde{\epsilon}_l)$, and the values $\mathrm{Var}(\epsilon_l)$ obtained using the noisy data $\mathbf{X}$, provided that the noise variance σ_w^2 determines a signal-to-noise ratio corresponding to an above-threshold estimation. Since $\mathrm{Var}(\epsilon_l)$ is evaluated using a noisy data matrix, its value depends on the particular noise realization; hence, the average value $\mathbb{E}[\mathrm{Var}(\epsilon_l)]$ has been considered in the simulations. As an example, consider Fig. 8, where the values of error variance are calculated for different noise variances σ_w^2 in the case of the $L = 4$-path channel defined by

$$\tau_0 = -1.075\ \mu\mathrm{s}, \qquad h_0 = 0.4 + j0.5 \quad (11a)$$
$$\tau_1 = 0.006\ \mu\mathrm{s}, \qquad h_1 = 1 + j0.39 \quad (11b)$$
$$\tau_2 = 0.358\ \mu\mathrm{s}, \qquad h_2 = 0.2 + j0.1 \quad (11c)$$
$$\tau_3 = 1.369\ \mu\mathrm{s}, \qquad h_3 = 0.15. \quad (11d)$$

The $\mathrm{RMSE}(\hat{\tau}_l) = \left(\mathbb{E}[(\tau_l - \hat{\tau}_l)^2]\right)^{1/2}$ obtained with an ESPRIT estimation of the multipath TOA is also shown, revealing the correctness of the error variance estimation.

3) Passing DP TOA Measurements to the KF: As a third phase of the EKAT algorithm, the DP has to be selected between the multipath components estimated with ESPRIT. Indeed, for each cell i and measurement time t, ESPRIT produces one set of TOA estimates per antenna port, i.e., $\Upsilon^{i,0}(t)$ and $\Upsilon^{i,1}(t)$. Each set of multipath TOA estimates contains $\hat{L}^{i,p}(t)$ TOA measurements. Hence, a selection mechanism that chooses the DP TOA among the $\hat{L}^{i,p}(t)$ time measurements in each set $\Upsilon^{i,p}(t)$ has to be implemented. Unfortunately, the selection mechanism cannot be a simple choice of the earliest TOA because of the possible estimated TOA outliers mentioned in Section IV-C1. For this reason, the DP TOA is selected in each set $\Upsilon^{i,p}(t)$ as the earliest TOA estimate that, compared with the previous tracked DP TOA $\hat{\zeta}_0(t-1)$ produced by the EKAT KF, does not determine a receiver speed higher than $v_{\max}^{(1)}$. This measurement selection strategy permits to discard the possible TOA outliers.

The selected ESPRIT estimations are passed to the EKAT KF by filling the entries of the measurement vector $\hat{\boldsymbol{z}}_E(t) \in \mathbb{R}^2$ with a DP TOA estimation for each antenna port. The TOA estimations taken from $\Upsilon^{i,p}(t)$, $p = \{0, 1\}$, and inserted in $\hat{\boldsymbol{z}}_E(t)$ are added to the synchronization delay Δt_s^i evaluated in the preprocessing phase for the particular considered cell.

Finally, the uncertainties of the ESPRIT TOA estimations are also passed to the KF, by filling the diagonal of the noise covariance matrix $\mathbf{R}(t) \in \mathbb{R}^{2\times 2}$ with the values evaluated as in (9) and corresponding to the particular TOA selected from the ESPRIT outcome $\Upsilon^{i,p}(t)$, for each antenna port $p = \{0, 1\}$.

4) DP TOA Tracking: The ESPRIT TOA estimation of Section IV-C1 is needed for separating the multipath and identifying the DP TOA. The EKAT algorithm takes this DP TOA estimation and tracks it with the aid of a classical KF, according to the procedure described in the following.

For each detected cell i, EKAT performs the tracking of the DP TOA along the different measurement times t using a state-space approach similar to [34]. More specifically, a state vector $\boldsymbol{\zeta}(t) \in \mathbb{R}^2$ and a measurement equation $\boldsymbol{z}_E(t) \in \mathbb{R}^2$ are defined for each received cell. The two dimensions of $\boldsymbol{\zeta}(t)$ represent, respectively, the DP TOA τ_0 and its rate of change $\Delta\tau_0$, i.e., $\boldsymbol{\zeta} = [\tau_0\ \ \Delta\tau_0]^T$. Each of the two dimensions of $\boldsymbol{z}_E(t)$ represents the DP TOA measurement performed from each received antenna port $p = 0$ and $p = 1$. As explained in Section IV-C3, this permits the filling of the estimated measurement vector $\hat{\boldsymbol{z}}_E(t)$ with the two DP TOA previously evaluated with ESPRIT, one per antenna port. This is the strategy used by EKAT to combine the TOA estimates evaluated from the two transmit antenna ports.

The evolution in time of the state $\boldsymbol{\zeta}(t)$ and its relation to the measurement equation $\boldsymbol{z}_E(t)$ are determined by the following recursive equations, inspired by the model of [35]

$$\boldsymbol{\zeta}(t) = \mathbf{F} \cdot \boldsymbol{\zeta}(t-1) + \boldsymbol{q}(t-1) \quad (12)$$
$$\boldsymbol{z}_E(t) = \mathbf{H} \cdot \boldsymbol{\zeta}(t) + \boldsymbol{r}(t) \quad (13)$$

where

$$\mathbf{F} = \begin{bmatrix} 1 & 1 \\ 0 & 1 \end{bmatrix} \text{ and } \mathbf{H} = \begin{bmatrix} 1 & 0 \\ 1 & 0 \end{bmatrix}. \quad (14)$$

The system equation of (12) defines a constant rate of change for the DP TOA, which implies a constant speed model, perturbed

by the process noise vector $\boldsymbol{q}(t) \in \mathbb{R}^2$. According to [35], the entries of $\boldsymbol{q}(t)$ are assumed zero-mean Gaussian RVs, with the following time-invariant covariance matrix

$$\mathbf{Q}(t) = \mathbf{Q} = q \begin{bmatrix} \frac{1}{3} & \frac{1}{2} \\ \frac{1}{2} & 1 \end{bmatrix} \qquad \forall\, t \tag{15}$$

where q may be set empirically during the KF tuning. Similarly, the entries of the measurement noise vector $\boldsymbol{r}(t) \in \mathbb{R}^2$ are assumed zero-mean Gaussian RVs as a consequence of the fact that $\hat{\boldsymbol{z}}_E(t)$ is filled with ESPRIT outcomes, which are affected by Gaussian noise, as mentioned in Section IV-C2 and demonstrated in [32]. Moreover, since $\hat{\boldsymbol{z}}_E(t)$ is filled with estimations corresponding to different antenna ports, these are assumed as affected by independent noise, resulting in a diagonal covariance matrix $\mathbf{R}(t) \in \mathbb{R}^{2\times 2}$, filled as described in Section IV-C3.

Having defined the state-space model of (12) and (13), and exploiting a conventional KF, it is possible to evaluate an estimate of the state vector $\boldsymbol{\zeta}(t)$ and to ultimately track the DP TOA. The KF recursive equations used for the DP TOA tracking are [36]

$$\hat{\boldsymbol{\zeta}}^{-}(t) = \mathbf{F} \cdot \hat{\boldsymbol{\zeta}}(t-1) \tag{16}$$

$$\hat{\mathbf{P}}^{-}(t) = \mathbf{F} \cdot \hat{\mathbf{P}}(t-1) \cdot \mathbf{F}^T + \mathbf{Q} \tag{17}$$

$$\mathbf{W}(t) = \hat{\mathbf{P}}^{-}(t) \cdot \mathbf{H}^T \cdot \left[\mathbf{R}(t) + \mathbf{H} \cdot \hat{\mathbf{P}}^{-}(t) \cdot \mathbf{H}^T\right]^{-1} \tag{18}$$

$$\hat{\boldsymbol{\zeta}}(t) = \hat{\boldsymbol{\zeta}}^{-}(t) + \mathbf{W}(t) \cdot \left[\hat{\boldsymbol{z}}_E(t) - \mathbf{H} \cdot \hat{\boldsymbol{\zeta}}^{-}(t)\right] \tag{19}$$

$$\hat{\mathbf{P}}(t) = [\mathbf{I}_2 - \mathbf{W}(t) \cdot \mathbf{H}] \cdot \hat{\mathbf{P}}^{-}(t) \tag{20}$$

where $\hat{\boldsymbol{z}}_E(t)$, $\hat{\boldsymbol{\zeta}}^{-}(t)$, $\hat{\mathbf{P}}^{-}(t)$, $\hat{\boldsymbol{\zeta}}(t)$, $\hat{\mathbf{P}}(t)$, and $\mathbf{W}(t)$ correspond to the estimated measurement vector, the predicted state, the predicted state covariance, the estimated state, the estimated state covariance, and the KF gain, respectively.

As a small recap for the EKAT flow, consider again Fig. 6. As one can see, the KF takes as an input $\hat{\boldsymbol{z}}_E(t)$, which is made of a selection of the TOA measurements performed with ESPRIT, together with the covariance matrix $\mathbf{R}(t)$, which quantifies the accuracy of the measurements in $\hat{\boldsymbol{z}}_E(t)$. The state estimated by the KF, which is denoted by $\hat{\boldsymbol{\zeta}}(t) = [\hat{\zeta}_0(t), \hat{\zeta}_1(t)]^T$, contains the tracked DP TOA $\hat{\zeta}_0(t)$, having a variance given by the upper left element of the state covariance matrix $\hat{\mathbf{P}}(t)$. Further details on the implementation and initialization of the KF used in the EKAT algorithm can be found in [17].

As a final remark, consider that the reception of the CRSs of a particular cell is not continuous, e.g., due to signal obstruction or due to the BS being too far for being detected. If the CRSs of a certain cell are not received for more than $D_{\max}$ consecutive measurements, the EKAT KF is stopped and reinitialized at the next available measurement.

D. Pseudorange Evaluation

The DP TOA estimation algorithms considered so far in the paper can be summarized as follows:

- IM, IL: CIR-based TOA estimators, not capable of dealing with NLOS cases, characterized by limited computational cost;
- TE, TN: CIR-based TOA estimators with reasonable computational cost and capability of dealing with multipath in both LOS and NLOS scenarios;
- EKAT: estimator particularly robust against multipath and intended for feasibility studies and analysis of the effects of multipath.

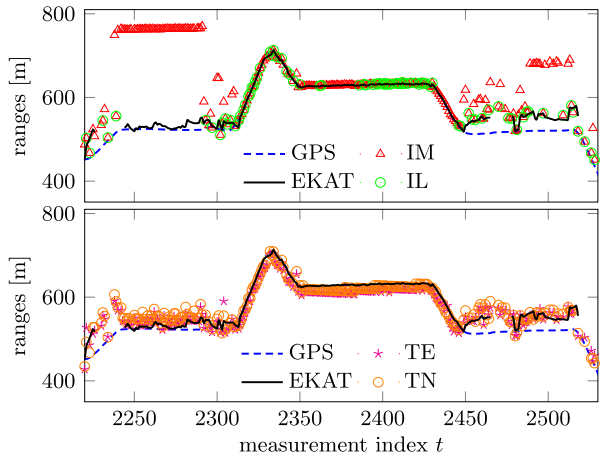

Fig. 9. Results of the range estimation using the CRSs of cell $N_{\mathrm{ID}}^{\mathrm{cell}} = 52$ operator 2 in a representative time interval. All the plotted values are actual ranges since they are already corrected for bias and drift. The ranging results of all the considered algorithms (i.e., EKAT, IM, IL, TE, and TN) are plotted. The GPS range is also shown as a reference.

By using the DP TOA estimated with the considered algorithms, the pseudorange for the ith detected cell ID at measurement time t was evaluated as

$$\hat{\rho}_i(t) = c \cdot \begin{cases} \Delta t_s^i + \hat{\tau}_x^i(t), & x \in \{\mathrm{IM}, \mathrm{IL}\} \text{ (Sec. IV-B)} \\ \Delta t_s^i + \Delta t_o + \hat{\tau}_x^i(t), & x \in \{\mathrm{TE}, \mathrm{TN}\} \text{ (Sec. IV-B)} \\ \hat{\zeta}_0^i(t), & \mathrm{EKAT} \text{ (Sec. IV-C).} \end{cases} \tag{21}$$

In (21), Δt_s^i is the delay introduced in respect to $t^{(U)}$ when synchronizing to cell i, $\hat{\tau}_x^i(t)$, $x \in \{\mathrm{IM}, \mathrm{IL}, \mathrm{TE}, \mathrm{TN}\}$ is the TOA estimation result given at time t from the CIR-based TOA estimators described in Section IV-B, and Δt_o is the constant offset correction needed for the TE and TN estimators. For the IM and IL estimators, $\hat{\tau}_x^i(t)$ is obtained selecting the earliest estimate between the two antenna ports as

$$\hat{\tau}_x^i(t) = \min_{p \in \{0,1\}} \left\{\hat{\tau}_x^{i,p}(t)\right\}, \; x \in \{\mathrm{IM}, \mathrm{IL}\} \tag{22}$$

where $\hat{\tau}_x^{i,p}(t)$ denotes the IM or IL TOA estimate at time t from antenna port p. Note that Δt_s^i is not added in the case of the EKAT estimator because it is already considered during the DP tracking, as highlighted in Section IV-C3.

The two plots of Fig. 9 shows the results of a range estimation using the five considered methods on the CRSs of cell $N_{\mathrm{ID}}^{\mathrm{cell}} = 52$ operator 2, for the same representative interval shown in Fig. 7. For a clearer understanding of each estimator's performance, all the plotted values are actual ranges, due to the application of the clock correction explained in Section VI. The GPS measured distance is also shown as a reference. As one can see, the benefits of the EKAT algorithm are evident since it

correctly tracks the DP, determining a consistent range estimate, which is almost equal to the GPS range measure. Conversely, the IM estimator is biased by multipath, particularly in the interval [2250, 2300], where the fourth received path (clearly visible in the plots of Fig. 7) is mismatched with the DP. Moreover, it is evident that the IL estimator gives substantial benefits compared with IM, being more robust against multipath detrimental effects, at the serious cost of discarding suspect NLOS measurements and, hence, producing fewer estimates (again evident in the interval [2250, 2300], where IL does not produce any outcome). Finally, the TE and TN estimators show good robustness in detecting the DP TOA.

V. Combining Pseudoranges From Multiple Cells of the Same Base Station

Since the aim of the performed pseudorange measurements is to calculate a position fix based on the BS position knowledge, a single range per BS is needed, instead of multiple ranges corresponding to each cell controlled by every BS. Hence, a method is needed for selecting a single pseudorange $\hat{\rho}_j^{\mathrm{BS}}(t)$ for each BS j out of the pseudoranges evaluated on a per-cell basis, as in (21).

More particularly, let $\bar{\mathcal{K}}_j$ be the set of the cell IDs controlled by BS j, and let $\mathcal{K}_j(t) \subseteq \bar{\mathcal{K}}_j$ be the set of cell IDs controlled by BS j that are visible by the receiver at the measurement time t. Then, consider the set $\Lambda_j(t)$, defined as the collection of cell IDs corresponding to the cells having pseudoranges that, compared with the previous estimation of the per-BS pseudorange $\hat{\rho}_j^{\mathrm{BS}}(t-1)$, do not imply a receiver movement with a speed higher than $v_{\max}^{(2)}$, i.e., $\Lambda_j(t) = \{i \in \mathcal{K}_j(t) : (1/T)|\hat{\rho}_j^{\mathrm{BS}}(t-1) - \hat{\rho}_i(t)| < v_{\max}^{(2)}\}$, where T is the interval between two measurements ($T = 1$ s in the proposed setup). The parameter $v_{\max}^{(2)}$ has to be set according to the expected receiver's maximum speed, which is determined by the environment and type of mobility (e.g., pedestrian or vehicular). If the per-BS pseudorange is selected using the pseudoranges of the cells in $\Lambda_j(t)$, robustness against estimated earlier-than-LOS TOA outliers is guaranteed.

A simple selection method is to choose the cell corresponding to the earliest estimated pseudorange. This method is the more intuitive, and it is used for combining pseudoranges evaluated with the IM, IL, TE, and TN algorithms. It has the drawback of not being robust against earlier-than-LOS TOA outliers. Another method, which is used for combining the EKAT pseudoranges, is based on the exploitation of the estimated variance of the tracked DP TOA. At every measurement time, for each BS, the cell corresponding to the measured range with the smallest estimated variance at that particular time is selected, where the estimated DP TOA variance is the upper left element $\hat{P}_{0,0}(t)$ of the state covariance matrix $\hat{\mathbf{P}}(t)$. This method may be more robust against TOA outliers since usually, they have a high estimated variance.

An example of the combination of multiple cell estimates is shown in Fig. 10 for BS 1 operator 2 in a representative time interval, using the variance method on the EKAT estimates. Again, for a clearer understanding of the combining performance, all the plotted values are actual ranges, corrected for time offset as explained in Section VI. The EKAT estimates pertaining to $N_{\mathrm{ID}}^{\mathrm{cell}} = \{51, 52, 53\}$, shown in the upper plot, are selected on the basis of their variance $\hat{P}_{0,0}(t)$, which is shown in the form of distance standard deviation in the bottom plot. The result constitutes the EKAT range estimate from BS 1 operator 2. As one can see, the earlier-than-LOS TOA outliers are discarded, e.g., at $t \simeq 2610$ and $t \simeq 2635$.

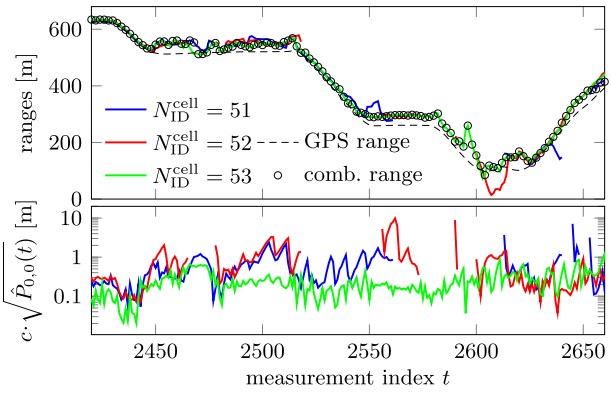

Fig. 10. Multiple cell combining of the EKAT pseudoranges for the cells of BS 1 operator 2. All the plotted values are actual ranges since already corrected for bias and drift.

VI. From Pseudorange to Range

Here, the relation between the measured pseudoranges and the actual distance estimates is explained. Suppose that the propagation channel is observed at the receiver, due to a LTE CRS transmissions from BS j, at the UTC epoch $t^{(U)}$. The corresponding estimated pseudorange is $\hat{\rho}_j^{\mathrm{BS}}(t)$, which is evaluated in respect to $t^{(U)}$ and, hence, corresponds to the UTC estimated DP TOA

$$\mathrm{TOA}_j(t) = t^{(U)} + \hat{\rho}_j^{\mathrm{BS}}(t)/c. \tag{23}$$

Consider then the unknown UTC epoch at which the CRS exploited for the TOA estimation was transmitted from the BS j, referred to as time of transmit (TOT), which can be expressed as

$$\mathrm{TOT}_j(t) = t^{(U)} + \varrho_j(t)/c + k \cdot \Delta T_{\mathrm{CRS}} \tag{24}$$

where the parameter $\varrho_j(t)/c$ is the unknown offset of the BS clock in respect to UTC time $t^{(U)}$, and $k \cdot \Delta T_{\mathrm{CSR}} = k \cdot 10$ ms, $k \in \mathbb{Z}$, is the ambiguity due to the CRS transmission periodicity. This ambiguity can be easily solved since the introduced offset is very large, i.e., $c \cdot \Delta T_{\mathrm{CRS}} = 3 \cdot 10^6$ m; hence, the value $k = 0$ was set. Finally, the actual distance estimate between the receiver and the transmitter, referred to as range, is given by

$$\hat{d}_j(t) = c \cdot (\mathrm{TOA}_j(t) - \mathrm{TOT}_j(t)) = \hat{\rho}_j^{\mathrm{BS}}(t) - \varrho_j(t). \tag{25}$$

Hence, the clock offset $\varrho_j(t)/c$ of the BS j must be known to the receiver to calculate the actual range estimate $\hat{d}_j(t)$. The proposed approach assumes that the BSs' clock offset in respect to UTC is available to the PE, enabling the correction of the pseudoranges $\hat{\rho}_j^{\mathrm{BS}}(t)$ to actual range estimations $\hat{d}_j(t)$.

A. BSs' *Clock Measurements in Real Implementations*

In a realistic implementation, several methods can be used for acquiring the knowledge of the BSs' clock properties, and ultimately of the clock offset $\varrho_j(t)/c$. As an example, the concept of LMUs may be employed. An LMU is a device with a known location that periodically performs TOA measurements from the received BSs. The knowledge of the LMU position, together with the position of each received BS, enables the evaluation of the BSs' clock offset $\varrho_j(t)/c$. These clock offset periodic measurements may be collected in a database, and exploited for the evaluation of the BSs' clock properties such as bias and drift, which can be passed to a PE that has to calculate the actual ranges on the basis of the TOA based pseudoranges. These LMUs may be fixed position devices spread in areas covered by the cellular network, may be installed on the BSs themselves, or may be mobile devices with known precise location.

B. BSs' *Bias and Drift Estimation*

Unfortunately, in our real field test, each BS clock offset $\varrho_j(t)$ was unknown; therefore, it was estimated by exploiting the GPS position fixes available for the receiver. Indeed, the knowledge of both the BS and the receiver position permits a straightforward calculation of the distance $d_j(t)$, which can be used to estimate $\varrho_j(t)$.

The instantaneous BS clock offset (expressed as a distance) $\varrho_j(t)$ is an unknown function of time t, and depends on several parameters, including the deviation of the BS clock from the nominal frequency, and environmental parameters such as temperature, power voltage, and pressure [37]. The BS clock offset was estimated by assuming an underlying linear model, i.e., $\varrho_j(t) = \mathfrak{D}_j + t \cdot \mathfrak{d}_j$, where $\mathfrak{D}_j$ represents the clock bias (measured in meters) and $\mathfrak{d}_j$ represents the clock drift (measured in meters per second), assumed constant. The linear model for the BSs' clock has been chosen as a first-order approximation, realizing a tradeoff between correct modeling and simplicity in the estimation of the BSs' clock parameters.

Let $\bar{\mathcal{T}}_j$ be the set of all measurement times in which both a receiver GPS fix [and hence the distance $d_j(t)$] and an LTE pseudorange $\hat{\rho}_j^{\mathrm{BS}}(t)$ from BS j were available during the real field test. Then, an estimate of $\mathfrak{D}_j$ and $\mathfrak{d}_j$ can be evaluated for any subset $\mathcal{T}_j \subseteq \bar{\mathcal{T}}_j$ as

$$(\hat{\mathfrak{D}}_j, \hat{\mathfrak{d}}_j) = \arg\min_{\mathfrak{d},\mathfrak{D}} \left\{ \sum_{t\in\mathcal{T}_j} \left| d_j(t) - \hat{\rho}_j^{\mathrm{BS}}(t) + \mathfrak{D} + t\cdot\mathfrak{d} \right|^2 \right\}. \tag{26}$$

The accuracy of the above estimation depends both on the accuracy of the LTE pseudoranges $\hat{\rho}_j^{\mathrm{BS}}(t)$ and on the number of considered measurements, i.e., on the cardinality of $\mathcal{T}_j$. The whole set $\bar{\mathcal{T}}_j$ and the EKAT pseudoranges were used to obtain the most precise bias and drift estimates.

VII. Tracking the Receiver Position

Several solutions may be chosen for the estimation of the position solution from the estimated LTE ranges. However, the proposal of a powerful PE is beyond the scope of this paper. A reader interested in powerful position tracking techniques and in their influence on the position solution may refer to [38]–[41] and references therein. In this paper, a classical extended KF (EKF) is adopted to estimate the receiver position.

An analysis of the geographical properties of the BSs used showed that their heights differ only slightly. In conjunction with the BS spread, which is large compared with the height differences, the situation is close to all BSs lying in one plane; hence, the rover position is solved in two dimensions only. The problem space is constrained to two dimensions by using local east-north-up coordinates (ENU), with the up component set to zero. A second-order model is used to describe the rover position. Hence, the state vector is $\boldsymbol{\xi}(t) = [\boldsymbol{p}(t), \dot{\boldsymbol{p}}(t), \ddot{\boldsymbol{p}}(t)]^T \in \mathbb{R}^6$, containing the 2-D rover position $\boldsymbol{p}(t) \in \mathbb{R}^2$, the 2-D rover speed $\dot{\boldsymbol{p}}(t) \in \mathbb{R}^2$, and the 2-D rover acceleration $\ddot{\boldsymbol{p}}(t) \in \mathbb{R}^2$. Whenever measurements to at least two BSs are available, a measurement update is performed. The constant acceleration second-order model leads to the following state transition model

$$\boldsymbol{\xi}(t) = \begin{bmatrix} 1 & 0 & \Delta t_p & 0 & \frac{1}{2}\Delta t_p^2 & 0 \\ 0 & 1 & 0 & \Delta t_p & 0 & \frac{1}{2}\Delta t_p^2 \\ 0 & 0 & 1 & 0 & \Delta t_p & 0 \\ 0 & 0 & 0 & 1 & 0 & \Delta t_p \\ 0 & 0 & 0 & 0 & 1 & 0 \\ 0 & 0 & 0 & 0 & 0 & 1 \end{bmatrix} \cdot \boldsymbol{\xi}(t-1) + \boldsymbol{q}_p(t-1) \tag{27}$$

where Δt_p is the elapsed time since the last position estimate at $t-1$, and $\boldsymbol{q}_p(t) \in \mathbb{R}^6$ is the zero-mean white Gaussian process noise of the position state equation, having constant covariance matrix $\mathbf{Q}_p = \mathbb{E}[\boldsymbol{q}_p(t)\boldsymbol{q}_p^H(t)]$. The measurement vector is $\boldsymbol{z}_p(t) = [z_{p,1}(t), \ldots, z_{p,N(t)}]^T$, where $N(t)$ is the number of received BSs at time t, and each component $z_{p,n}(t)$ is the measured range between the receiver and the nth BS, which is given by the nonlinear observation model, i.e.,

$$z_{p,n}(t) = \left\| \boldsymbol{p}_{\mathrm{BS}}^n - \boldsymbol{p}(t) \right\|, \quad n = 1, \ldots, N(t-1) \tag{28}$$

with the vector $\boldsymbol{p}_{\mathrm{BS}}^n \in \mathbb{R}^2$ representing the known 2-D location of the nth received BS. According to [36], the linearization of (28) around the predicted position $\hat{\boldsymbol{p}}^-(t)$, which is produced by the EKF, leads to the following linear observation model

$$\mathbf{H}_p(t) = \begin{bmatrix} \left(\hat{\boldsymbol{p}}^-(t) - \boldsymbol{p}_{\mathrm{BS}}^1\right)^T \Big/ \left\| \boldsymbol{p}_{\mathrm{BS}}^1 - \hat{\boldsymbol{p}}^-(t) \right\| & \mathbf{0}_4^T \\ \left(\hat{\boldsymbol{p}}^-(t) - \boldsymbol{p}_{\mathrm{BS}}^2\right)^T \Big/ \left\| \boldsymbol{p}_{\mathrm{BS}}^2 - \hat{\boldsymbol{p}}^-(t) \right\| & \mathbf{0}_4^T \\ \vdots & \vdots \\ \left(\hat{\boldsymbol{p}}^-(t) - \boldsymbol{p}_{\mathrm{BS}}^{N(t)}\right)^T \Big/ \left\| \boldsymbol{p}_{\mathrm{BS}}^{N(t)} - \hat{\boldsymbol{p}}^-(t) \right\| & \mathbf{0}_4^T \end{bmatrix} \in \mathbb{R}^{N(t)\times 6}. \tag{29}$$

The matrix of (29) is evaluated at every iteration of the EKF, which produces at each step an estimate $\hat{\boldsymbol{p}}(t)$ of the receiver position. The measurements are supposed to be corrupted by a zero-mean Gaussian noise vector $\boldsymbol{r}_p(t) \in \mathbb{R}^{N(t)}$, having covariance matrix $\mathbf{R}_p = \mathbb{E}[\boldsymbol{r}_p(t)\boldsymbol{r}_p^H(t)]$. The matrices $\mathbf{Q}_p$ and $\mathbf{R}_p$ were supposed time invariant and were tuned empirically.

VIII. Results

Here, the ranging and positioning results obtained with the live data captured using the setup of Section III are summarized. Pseudorange estimations were first performed from the detected cells with the algorithms of Section IV, namely IDFT-MAX (IM), IDFT-LOS (IL), TEMOS (TE), TNR (TN), and EKAT (E). Then, cell pseudoranges were combined with the method of Section V, in order to obtain a single pseudorange for each BS, which was corrected for clock bias and drift, according to the procedure of Section VI. Finally, these range estimates were used in the position tracking filter of Section VII to evaluate a position estimate.

A. Parameters Used

The IM estimator was run as described in Section IV-B, whereas for the IL algorithm the number of searched CIR peaks was set to $N_{\mathrm{IL}} = 3$. The TEMOS algorithm was run in its TEMOS-E flavor, i.e., by only considering the PDP samples between the first and the highest, and the simplified CAICF penalty function was employed [23]. The TNR-based TOA estimation employed a target early detection probability of 10^{-3} in order to evaluate the TNR based on the procedure described in [24]. The used TNR depends also on the number $2N_{\mathrm{tot}}$ of PDP samples available, which is ultimately determined by the LTE bandwidth configuration. The EKAT algorithm was run with parameters similar to those used in [17], in particular: $D_{\max} = 3$, $\bar{m} = 0.48$, $v_{\max}^{(1)} = 70$ m/s, $v_{\max}^{(2)} = 30$ m/s, $q = 5 \cdot 10^{-19}$. Finally, the position tracking EKF used the following process and measurement noise covariance matrices:

$$\mathbf{Q}_p = \mathrm{diag}\left\{\left[q_1 \Delta t_p^2,\ q_1 \Delta t_p^2,\ q_2 \Delta t_p^2,\ q_2 \Delta t_p^2,\ q_3,\ q_3\right]\right\} \quad (30)$$

$$\mathbf{R}_p = \mathrm{diag}\left\{[r, r, \ldots, r]\right\} \in \mathbb{C}^{N(t)\times N(t)} \quad (31)$$

where $q_1 = (6\ \mathrm{m})^2$, $q_2 = (0.5\ \mathrm{m/s})^2$, and $q_3 = (0.0092\ \mathrm{m/s}^2)^2$. In (31), the values of r differ depending on the adopted ranging algorithm. The value of $r = (40\ \mathrm{m})^2$ was set in the IM, IL, TE, and TN cases. In the EKAT case, a smaller value of $r = (10\ \mathrm{m})^2$ was used, in order to give more trust to the ranges evaluated by this algorithm.

B. Ranging Results

The range estimates $\hat{d}_j(t)$ were compared with the GPS-based ranges $d_j(t)$ in order to produce error statistics, and ultimately, to evaluate the performance of each used pseudorange estimator. Empirical cumulative density functions (cdfs) of the ranging absolute error were evaluated as $P(|\mathcal{E}_d| < \varepsilon)$ for each BS and each estimator, where $\mathcal{E}_d = \hat{d} - d$. Two different error definitions were adopted for evaluating the cdfs.

The first type of error considered, denoted with $\mathcal{E}_d^{\mathrm{est}}$, is calculated considering separately all the estimates produced by the five ranging algorithms. The corresponding error probability abscissas, defined as the value ε_p such that $P(|\mathcal{E}_d^{\mathrm{est}}| < \varepsilon_p) = p$, for $p = \{0.5, 0.95\}$, were also evaluated. The results are shown for selected BSs in Fig. 11(a). The best error performance is always obtained by the EKAT estimator, which exhibits an $\varepsilon_{0.5}$ and an $\varepsilon_{0.95}$ that are always smaller than the corresponding values of the other estimators. Moreover, it is evident that the IL estimator obtains a better estimation of the range than the IM estimator, sometimes even comparable with that of EKAT (e.g., for BS 5 operator 1). The $\varepsilon_{0.95}$ performance of TE and TN when calculated on the basis of $\mathcal{E}_d^{\mathrm{est}}$ is better compared with that of IL but always worse than that of EKAT. A complete comparison is shown in Table II, where the values of ε_p obtained for all the BSs are reported for all the estimators. The results show that the $p = 0.5$ performance of EKAT and IL are comparable, whereas at $p = 0.95$ IL presents a higher error probably because it cannot completely handle multipath effects. Similarly, TE and TN perform better than IL and worse than EKAT at $p = 0.95$ but also worse than IL at $p = 0.5$. Finally, as expected, the IM estimator shows the worst results since by definition it cannot face multipath.

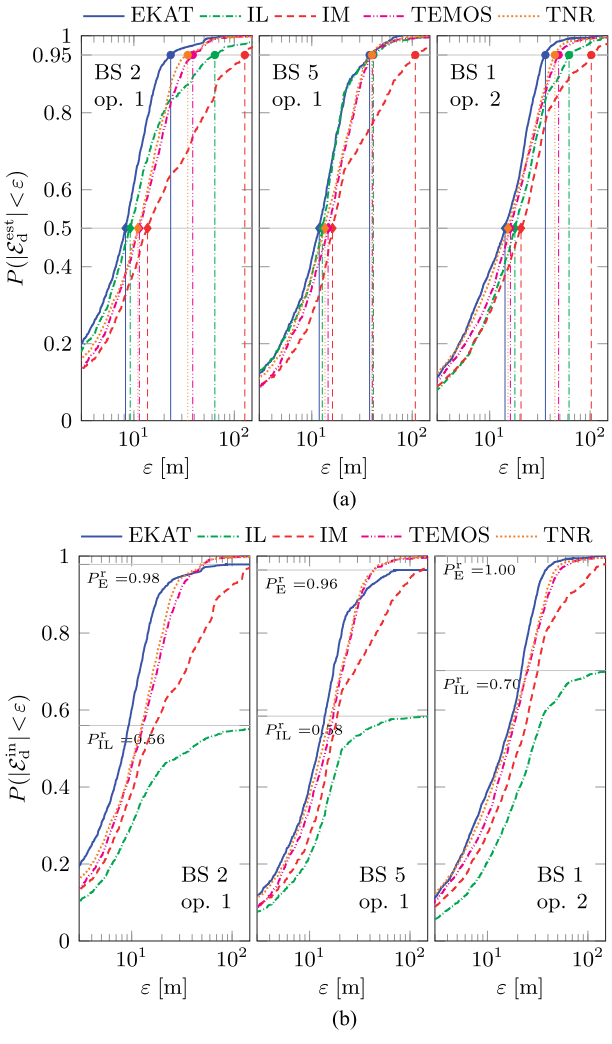

Fig. 11. CDFs of the ranging error (a) $\mathcal{E}_d^{\mathrm{est}}$ and (b) $\mathcal{E}_d^{\mathrm{in}}$ for selected BSs of operators 1 and 2. In (a), the values $\varepsilon_{0.5}$ (♦) and $\varepsilon_{0.95}$ (●) are also highlighted. In (b), the values of P_x^{r}, $x \in \{E, \mathrm{IL}\}$, are also shown.

The cdfs for the second type of error, denoted with $\mathcal{E}_d^{\mathrm{in}}$, are calculated similarly to the ones of $\mathcal{E}_d^{\mathrm{est}}$, with the exception that they are plotted as a percentage of the common number of input data. This kind of comparison is needed for including in the error statistics the fact that, differently from IM, TE, and TN,

TABLE II
RANGING ERRORS STATISTICS FOR $\mathcal{E}_d^{\text{est}}$ AND COVERAGE VALUES FOR IL AND EKAT

Op.	BS	$\varepsilon_{0.5}^{\text{IM}}$ [m]	$\varepsilon_{0.95}^{\text{IM}}$ [m]	$\varepsilon_{0.5}^{\text{IL}}$ [m]	$\varepsilon_{0.95}^{\text{IL}}$ [m]	$\varepsilon_{0.5}^{\text{E}}$ [m]	$\varepsilon_{0.95}^{\text{E}}$ [m]	$\varepsilon_{0.5}^{\text{TE}}$ [m]	$\varepsilon_{0.95}^{\text{TE}}$ [m]	$\varepsilon_{0.5}^{\text{TN}}$ [m]	$\varepsilon_{0.95}^{\text{TN}}$ [m]	P_{IL}^{r}	P_{E}^{r}
1	1	11.49	56.47	8.65	53.34	10.16	50.68	14.41	54.25	14.29	62.46	0.71	0.98
	2	13.67	127.20	9.20	63.97	8.26	23.24	11.34	38.56	10.96	34.37	0.56	0.98
	3	18.51	175.26	11.62	107.99	8.94	47.96	21.64	86.75	15.73	72.71	0.67	0.89
	5	16.07	107.38	12.73	41.06	11.86	37.64	14.53	40.06	13.54	39.69	0.58	0.96
	6	3.37	65.26	3.03	19.53	3.40	12.20	7.84	24.19	7.85	19.76	0.66	0.97
2	1	20.52	102.74	17.82	61.71	14.21	35.90	16.09	48.58	15.23	44.57	0.70	1.00
	2	17.07	208.17	12.16	59.68	11.19	51.59	21.78	98.93	20.01	82.08	0.53	0.86
	3	23.12	140.02	15.92	51.09	17.36	43.53	22.78	62.12	19.04	52.41	0.58	0.99

EKAT and IL do not produce an estimate for each input measurement. EKAT requires some measurements to be initialized, and it may be restarted in case of more than $D_{\max}$ missing measurements; hence, it may happen that a measurement does not correspond to an estimate. Similarly, IL discards a measurement in the case of a NLOS situation, and this happens quite frequently in the considered data set. With this error definition an empirical probability P_x^r, $x \in \{\text{IL}, E\}$ can be defined, for the likelihood that the particular algorithm will produce a range estimate when a measurement is available. Note that the number of estimates produced by IM, TE, and TN is always equal to number of input measurements; hence, $P_{\text{IM}}^r = P_{\text{TE}}^r = P_{\text{TN}}^r = 1$. The corresponding results are shown in Fig. 11(b) for the same cases considered in Fig. 11(a). As one can see, EKAT obtains the best tradeoff between small error performance and an unlikely outage, whereas IL seriously suffers of a performance reduction due to the high number of discarded measurements. As an example, consider the case of BS 5 operator 1, represented in the middle plots of Fig. 11. According to $\mathcal{E}_d^{\text{est}}$ [see Fig. 11(a)], IL and EKAT exhibit almost the same performance. Considering $\mathcal{E}_d^{\text{in}}$ [see Fig. 11(b)], it is evident that the statistics of IL pertain just to 58% of the possible range estimations, whereas EKAT produces estimates of the same quality in 96% of cases. The values of P_x^r, $x \in \{\text{IL}, E\}$, for all the received BSs are reported in the two right columns of Table II.

C. Positioning Results

The evaluated ranges were used in the positioning algorithm described in Section VII, obtaining the results shown in Fig. 13. Each plot corresponds to a different ranging technique. Each marker in each plot is a position estimate, where the different marker types represent the number of BSs $N(t)$ used for evaluating that particular position fix. By using the GPS position fixes gathered during the live measurements as the true positions $\boldsymbol{p}$, a positioning error was defined as $\mathcal{E}_p = \|\hat{\boldsymbol{p}} - \boldsymbol{p}\|$. Error cdfs were evaluated as $P(\mathcal{E}_p < \varepsilon)$, which are shown in Fig. 12. The same two error definitions of the ranging results section are adopted, namely the error $\mathcal{E}_p^{\text{est}}$, which considers all the estimates produced by the positioning algorithm, and the error $\mathcal{E}_p^{\text{in}}$, which represents the results as a percentage of the common number of inputs. Using the error definition of $\mathcal{E}_p^{\text{est}}$, error probability abscissas were also evaluated as $P(\mathcal{E}_p^{\text{est}} < \varepsilon_p) = p$, $p = \{0.5, 0.95\}$, and an RMS positioning error was evaluated as $(\mathbb{E}[(\mathcal{E}_p^{\text{est}})^2])^{1/2}$. As usually done in positioning contexts, $\varepsilon_{0.5}$ and $\varepsilon_{0.95}$ are referred to as circular error probability (CEP) and

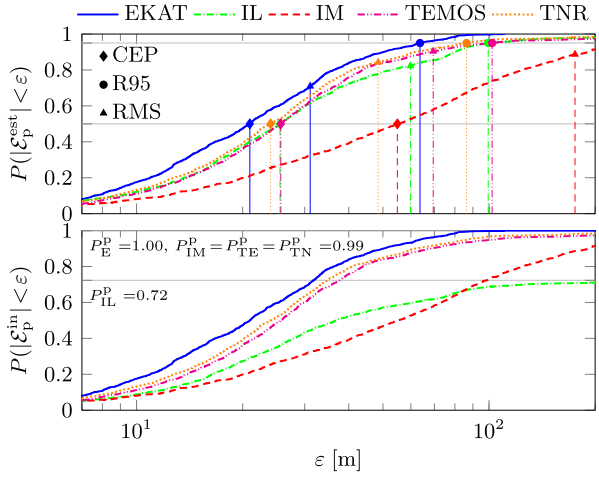

Fig. 12. CDFs of the positioning errors $\mathcal{E}_p^{\text{est}}$ and $\mathcal{E}_p^{\text{in}}$ for the considered ranging techniques. The CEP, R95, and RMS statistics are shown for $\mathcal{E}_p^{\text{est}}$, and the position fix probability P^p is shown in the $\mathcal{E}_p^{\text{in}}$ plot.

95% radius (R95), respectively. Similarly to Section VIII-C, the error definition $\mathcal{E}_p^{\text{in}}$ leads to a position fix probability P^p.

The positioning result obtained with the IM range estimator, not shown for space reasons, gave a CEP of 54 m, an RMS of 175 m, and an R95 of 460 m. As explained in Section IV-B, the IM estimator produces the typical timing outputs of a communications module. Hence, the poor positioning results of IM demonstrate the need for appropriate processing at the receiver in order to correctly extract the TOA of a signal for positioning purposes.

The positioning result obtained with the IL range estimator is shown in Fig. 13(a), and demonstrates that a simple NLOS rejection algorithm is sufficient to drastically improve the quality of the position fixes provided, resulting in a good CEP figure of 25.53 m. However, this comes at the cost of a consistent decrease in the positioning yield, which can seriously impact the positioning result, particularly in situations where very few BSs are visible and most of them present NLOS propagation. This is the case for the regions highlighted by the orange dashed ellipses of Fig. 13(a). There, IL probably discards the majority of the measurements because of suspect NLOS cases, passing to the PE only a limited number of pseudoranges, resulting in a poor or totally absent positioning fix. The reduced positioning yield of IL is evident in Fig. 13(a) from the low number of position fixes produced with $N(t) \geq 4$ BSs, and from its small position fix probability $P_{\text{IL}}^p = 0.72$, as shown in the bottom plot of Fig. 12.

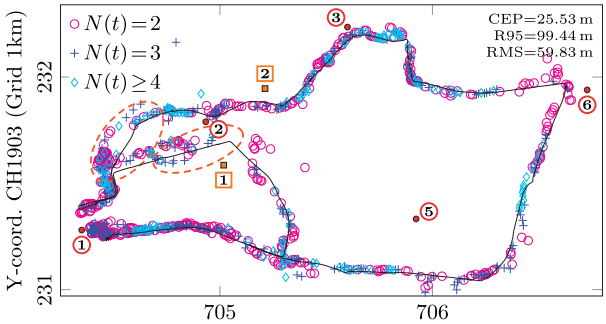

(a)

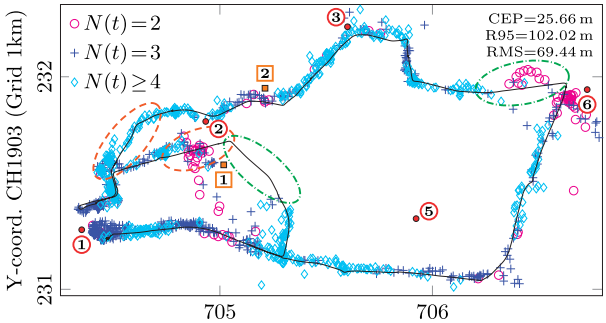

(b)

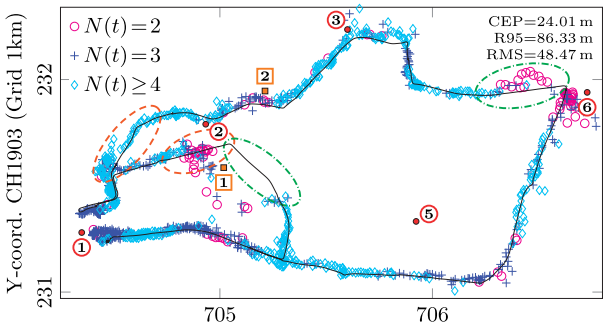

(c)

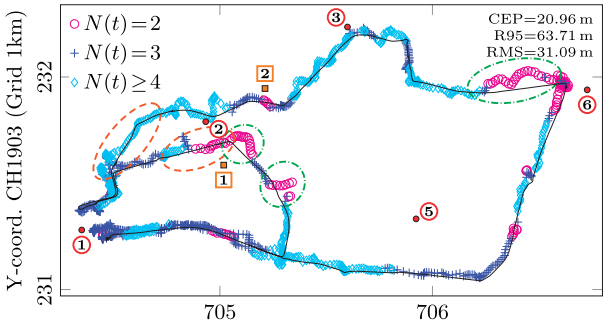

(d)

Fig. 13. Positioning solution for the (a) IL, (b) TE, (C) TN, and (d) EKAT ranging techniques. One marker corresponds to a position estimate, obtained with a number $N(t)$ of detected BSs. In each plot, the line ——, the circular markers, and the square markers indicate the test route, the BSs of operator 1, and the BSs of operator 2, respectively.

The positioning results obtained with the TE and TN estimators are shown in Fig. 13(b) and (c). The quality of the estimates in the regions where IL fails is improved in both cases, with the position fixes of TE and TN achieving a CEP similar to IL, and with TN achieving an improved RMS of 48.47 m. In contrast to IL, these estimators are capable of dealing also with NLOS cases; hence, their positioning performance presents a greater yield, as the bottom plot of Fig. 12 shows. The regions where TE and TN have positioning problems are highlighted with green dash-dotted ellipses, and these are mainly due to signals from too few BSs being available.

Finally, Fig. 13(d) shows the positioning results obtained using the ranges estimated with the EKAT algorithm. As one can see from the top plot of Fig. 12, EKAT achieves the best performance among the considered ranging techniques, with a CEP of 20.96 m, an R95 of 63.71 m, and an RMS of 31.09 m. Moreover, EKAT offers the best coverage, achieving a null outage probability in the considered scenario, and the highest number of position fixes obtained with $N(t) \geq 4$ BSs. The quality of the position fixes achieved by EKAT in the regions where IL fails is remarkable, due to the ability of EKAT to cope with the detrimental effects of multipath. Finally, most of the regions where the positioning fixes produced with the EKAT ranges have a low quality, are characterized by a low number of BSs visible, as the green dash-dotted ellipses of Fig. 13(d) highlight.

IX. Conclusion

A localization method that exploits the LTE downlink signals has been proposed and validated in the field for tracking the position of a receiver in a vehicle. A data gathering platform has been developed for opportunistically collecting the LTE signals throughout the test route. TOA measurements of the LTE cell-specific reference signal have been exploited to calculate the pseudoranges from the received BSs. The EKAT algorithm, which is capable of reducing the detrimental effects of multipath, has been used for performing the estimation of the LTE signals TOA. Moreover, a combination of the received signals in the time, frequency, spatial, and cell ID domains has been exploited for improving the timing estimates. The pseudoranges have been corrected for BSs' clock bias and drift, previously estimated, and used in a positioning filter. A CEP of 25.53 m and an RMS of 59.83 m with a coverage of the 72% have been obtained using a simple CIR-based timing algorithm with NLOS rejection, whereas a CEP of 24.01 m and an RMS of 48.47 m with full coverage have been obtained using a TNR-based TOA estimator. This demonstrates the feasibility of LTE-based positioning systems, even with simple signal processing at the receiver. Improved CEP, RMS (20.96 and 31.09 m, respectively), and universal coverage throughout the test have been obtained with the more powerful EKAT algorithm, demonstrating its benefits in correctly detecting the DP in environments characterized by multipath propagation. The proposed approach demonstrates that positioning with LTE signals is possible, even without transmission of the LTE PRS. Improvements are easily achievable in the positioning performance, e.g., employing a better navigation filter, and exploiting the forthcoming wider deployment of LTE cells/micro-cells/pico-cells, and the transmission of LTE channels with a wider bandwidth. To the best of the authors' knowledge, this is the first contribution proposing a real field validation of a positioning approach that uses opportunistically the LTE downlink signals.

REFERENCES

[1] R. Zakavat, S. Kansal, and A. Levesque, "Wireless positioning systems: Operation, application, and comparison," in *Handbook of Position Location: Theory, Practice and Advances*, R. Zekavat and R. Buehrer, Eds. New York, NY, USA: Wiley, 2012, pp. 3–23.

[2] M. Win *et al.*, "Network localization and navigation via cooperation," *IEEE Commun. Mag.*, vol. 49, no. 5, pp. 56–62, May 2011.

[3] Z. F. Syed, P. Aggarwal, X. Niu, and N. El-Sheimy, "Civilian vehicle navigation: Required alignment of the inertial sensors for acceptable navigation accuracies," *IEEE Trans. Veh. Technol.*, vol. 57, no. 6, pp. 3402–3412, Nov. 2008.

[4] C. Yang and H. rong Shao, "WiFi-based indoor positioning," *IEEE Commun. Mag.*, vol. 53, no. 3, pp. 150–157, Mar. 2015.

[5] F. Gustafsson and F. Gunnarsson, "Mobile positioning using wireless networks: Possibilities and fundamental limitations based on available wireless network measurements," *IEEE Signal Process. Mag.*, vol. 22, no. 4, pp. 41–53, Jul. 2005.

[6] *Evolved Universal Terrestrial Radio Access (E-UTRA); Physical channels and modulation (Release 11)*, Third-Generation Partnership Project, 3GPP TS 36.211, V11.0.0, Oct. 2012.

[7] K. Ranta-aho and Z. Shen, "User equipment positioning," in *LTE—The UMTS Long Term Evolution*, S. Sesia, I. Toufik, and M. Baker, Eds. New York, NY, USA: Wiley, 2009, pp. 423–436.

[8] J. A. del Peral-Rosado, J. A. López-Salcedo, G. Seco-Granados, F. Zanier, and M. Crisci, "Achievable localization accuracy of the positioning reference signal of 3GPP LTE," in *Proc. Int. Conf. Localization GNSS*, Jun. 2012, pp. 1–6.

[9] J. A. del Peral-Rosado, J. A. López-Salcedo, G. Seco-Granados, F. Zanier, and M. Crisci, "Joint maximum likelihood time-delay estimation for LTE positioning in multipath channels," *EURASIP J. Adv. Signal Process.*, vol. 2014, no. 1, p. 33, 2014.

[10] J. A. del Peral-Rosado *et al.*, "Comparative results analysis on positioning with real LTE signals and low-cost hardware platforms," in *Proc. 7th ESA Workshop Satellite Navig. Technol. Europ. Workshop GNSS Signals Signal Process.*, Dec. 2014, pp. 1–8.

[11] C. Gentner, E. Munoz, M. Khider, E. Staudinger, S. Sand, and A. Dammann, "Particle filter based positioning with 3GPP-LTE in indoor environments," in *Proc. IEEE/ION Position Location Navig. Symp.*, Apr. 2012, pp. 301–308.

[12] C. Gentner, S. Sand, and A. Dammann, "OFDM indoor positioning based on TDOAs: Performance analysis and experimental results," in *Proc. Int. Conf. Local. GNSS*, Jun. 2012, pp. 1–7.

[13] J. A. del Peral-Rosado, J. A. López-Salcedo, G. Seco-Granados, P. Crosta, F. Zanier, and M. Crisci, "Downlink synchronization of LTE base stations for opportunistic ToA positioning," in *Proc. Int. Conf. Local. GNSS*, Jun. 2015, pp. 1–6.

[14] S. Bartoletti, A. Conti, and M. Win, "Passive radar via LTE signals of opportunity," in *Proc. IEEE Int. Conf. Commun. Workshops*, Jun. 2014, pp. 181–185.

[15] A. Dammann, S. Sand, and R. Raulefs, "On the benefit of observing signals of opportunity in mobile radio positioning," in *Proc. 9th Int. ITG Conf. Systems, Commun. Coding*, Jan. 2013, pp. 1–6.

[16] F. Knutti, M. Sabathy, M. Driusso, H. Mathis, and C. Marshall, "Positioning using LTE signals," in *Proc. Europ. Navig. Conf.*, Apr. 2015, pp. 1–8.

[17] M. Driusso, F. Babich, F. Knutti, M. Sabathy, and C. Marshall, "Estimation and tracking of LTE signals time of arrival in a mobile multipath environment," in *Proc. 9th Int. Symp. Image Signal Process. Anal.*, Sep. 2015, pp. 276–281.

[18] OFCOM—Location of Radio Transmitters, Swiss Federal Office of Communications (OFCOM), Accessed: Nov. 3, 2015. [Online]. Available: http://www.bakom.admin.ch/themen/frequenzen/00652/00699/index.html?lang=en

[19] G. L. Stüber, *Principles of Mobile Communication*, 2nd ed. Boston, MA, USA: Kluwer, 2001.

[20] Y. Liu, Z. Tan, H. Hu, L. Cimini, and G. Li, "Channel estimation for OFDM," *IEEE Commun. Surveys Tuts.*, vol. 16, no. 4, pp. 1891–1908, 4th Quart. 2014.

[21] A. Ancora, S. Sesia, and A. Gorokhov, "Reference signals and channel estimation," in *LTE—The UMTS Long Term Evolution*, S. Sesia, I. Toufik, and M. Baker, Eds. New York, NY, USA: Wiley, 2009, pp. 165–187.

[22] F. Benedetto, G. Giunta, and E. Guzzon, "Enhanced TOA-based indoor-positioning algorithm for mobile LTE cellular systems," in *Proc. 8th Workshop Position. Navig. Commun.*, Apr. 2011, pp. 137–142.

[23] A. Giorgetti and M. Chiani, "Time-of-arrival estimation based on information theoretic criteria," *IEEE Trans. Signal Process.*, vol. 61, no. 8, pp. 1869–1879, Apr. 2013.

[24] D. Dardari, C.-C. Chong, and M. Win, "Threshold-based time-of-arrival estimators in UWB dense multipath channels," *IEEE Trans. Commun.*, vol. 56, no. 8, pp. 1366–1378, Aug. 2008.

[25] B. Yang, K. Letaief, R. Cheng, and Z. Cao, "Channel estimation for OFDM transmission in multipath fading channels based on parametric channel modeling," *IEEE Trans. Commun.*, vol. 49, no. 3, pp. 467–479, Mar. 2001.

[26] X. Li and K. Pahlavan, "Super-resolution TOA estimation with diversity for indoor geolocation," *IEEE Trans. Wireless Commun.*, vol. 3, no. 1, pp. 224–234, Jan. 2004.

[27] N. Alsindi, X. Li, and K. Pahlavan, "Analysis of time of arrival estimation using wideband measurements of indoor radio propagations," *IEEE Trans. Instrum. Meas.*, vol. 56, no. 5, pp. 1537–1545, Oct. 2007.

[28] D. G. Manolakis, V. K. Ingle, and S. M. Kogon, *Statistical and Adaptive Signal Processing: Spectral Estimation, Signal Modeling, Adaptive Filtering, and Array Processing*. Norwood, MA, USA: Artech House, 2005.

[29] A. Liavas and P. Regalia, "On the behavior of information theoretic criteria for model order selection," *IEEE Trans. Signal Process.*, vol. 49, no. 8, pp. 1689–1695, Aug. 2001.

[30] A. Liavas, P. Regalia, and J.-P. Delmas, "Blind channel approximation: Effective channel order determination," *IEEE Trans. Signal Process.*, vol. 47, no. 12, pp. 3336–3344, Dec. 1999.

[31] J. Via, I. Santamaria, and J. Perez, "Effective channel order estimation based on combined identification/equalization," *IEEE Trans. Signal Process.*, vol. 54, no. 9, pp. 3518–3526, Sep. 2006.

[32] F. Li, R. Vaccaro, and D. Tufts, "Performance analysis of the state-space realization (TAM) and ESPRIT algorithms for DOA estimation," *IEEE Trans. Antennas Propag.*, vol. 39, no. 3, pp. 418–423, Mar. 1991.

[33] X. Xu, Y. Jing, and X. Yu, "Subspace-based noise variance and SNR estimation for OFDM systems," in *Proc. IEEE Wireless Commun. Netw. Conf.*, Mar. 2005, vol. 1, pp. 23–26.

[34] T. Jost, W. Wang, U. Fiebig, and F. Perez-Fontan, "Detection and tracking of mobile propagation channel paths," *IEEE Trans. Antennas Propag.*, vol. 60, no. 10, pp. 4875–4883, Oct. 2012.

[35] J. Salmi, A. Richter, and V. Koivunen, "Detection and tracking of MIMO propagation path parameters using state-space approach," *IEEE Trans. Signal Process.*, vol. 57, no. 4, pp. 1538–1550, Apr. 2009.

[36] Y. Bar-Shalom, X. R. Li, and T. Kirubarajan, *Estimation With Applications to Tracking and Navigation: Theory Algorithms and Software*. New York, NY, USA: Wiley, Apr. 2001.

[37] B. Denis, J.-B. Pierrot, and C. Abou-Rjeily, "Joint distributed synchronization and positioning in UWB *ad hoc* networks using TOA," *IEEE Trans. Microw. Theory Tech.*, vol. 54, no. 4, pp. 1896–1911, Jun. 2006.

[38] Y. Shen and M. Win, "Fundamental limits of wideband localization—Part I: A general framework," *IEEE Trans. Inf. Theory*, vol. 56, no. 10, pp. 4956–4980, Oct. 2010.

[39] Y. Shen, H. Wymeersch, and M. Win, "Fundamental limits of wideband localization—Part II: Cooperative networks," *IEEE Trans. Inf. Theory*, vol. 56, no. 10, pp. 4981–5000, Oct. 2010.

[40] Y. Shen, S. Mazuelas, and M. Win, "Network navigation: Theory and interpretation," *IEEE J. Sel. Areas Commun.*, vol. 30, no. 9, pp. 1823–1834, Oct. 2012.

[41] S. Mazuelas, Y. Shen, and M. Win, "Belief condensation filtering," *IEEE Trans. Signal Process.*, vol. 61, no. 18, pp. 4403–4415, Sep. 2013.

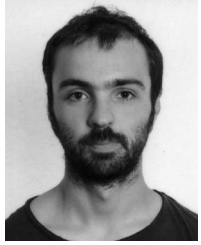

Marco Driusso was born in San Vito al Tagliamento, Italy, in 1987. He received the Bachelor's and Master's degrees in telecommunications engineering (*summa cum laude*) and the Ph.D. degree from the University of Trieste, Trieste, Italy, in 2009, 2012, and 2016, respectively.

For his doctoral studies, he conducted a three-year research project on the processing of Long-Term Evolution signals for positioning. From May 2011 to October 2011, he was with the Communications Research Group, University of Southampton, Southampton, UK, as a Visiting Student, working on space–time coding schemes and orthogonal frequency-division multiplexing. He is currently with u-blox Italia S.p.A., Sgonico, Italy, where he develops signal processing algorithms for cellular positioning.

Chris Marshall received the M.A. degree in natural and electrical sciences from the University of Cambridge, Cambridge, UK, in 1980 and the Ph.D. degree from Imperial College London, London, UK in 1985.

In 1980, after his master's studies, he joined Philips Research Laboratories. He pursued and led a variety of research and advanced development activities with Philips in the UK and, from 1991 to 1996, in Germany. He worked on one of the first chipsets for Global System for Mobile Communications digital cellular transceivers, and on the air-interface standard IEEE 802.15.4 used for machine-to-machine wireless connectivity systems such as ZigBee. From 2003, he led Philips' creation of software GPS technology and was the Chief Technology Officer of the NXP spin-out Geotate, which was acquired by u-blox UK Ltd., Reigate, UK, in 2009. He is currently creating cellular positioning product technology.

Dr. Marshall is a Fellow of The Institution of Engineering and Technology.

Mischa Sabathy was born in Wetzikon, Switzerland, in 1987. He received the B.Sc. degree in electrical engineering from Hochschule für Technik Rapperswil (HSR), Rapperswil, Switzerland, in 2013.

Since 2013, he has been with the Institute for Communication Systems, HSR, where he has been engaged in research on baseband signal processing and physical-layer aspects of microwave applications.

Fabian Knutti was born in Maennedorf, Switzerland, in 1982. He received the B.Sc. and M.Sc. degrees in electrical engineering from Hochschule für Technik Rapperswil (HSR), Rapperswil, Switzerland, in 2011 and 2014, respectively.

He is currently with the Institute for Communication Systems, HSR, where he is engaged in research on baseband signal processing and microwave communication systems.

Heinz Mathis (M'02) was born in Zurich, Switzerland, in 1968. He received the Diploma and Ph.D. degrees in electrical engineering from the Swiss Federal Institute of Technology (ETH), Zurich, in 1993 and 2001, respectively.

From 1993 to 1997, he was a Digital Signal Processing and Radio-Frequency Engineer with different companies in Switzerland and England. From 1997 to 2001, he was a Research Assistant with the Signal and Information Processing Laboratory, ETH Zurich. Since 2002, he has been a Professor of wireless communications with Hochschule für Technik Rapperswil (HSR), Rapperswil, Switzerland. His research interests include signal processing for wireless communication and navigation systems.

Fulvio Babich (SM'02) received the Doctoral degree in electrical engineering from the University of Trieste, Trieste, Italy, in 1984.

From 1984 to 1987, he was with the Research and Development Department of Telettra, working on optical communications. Then, he was with Zeltron (Electrolux group), where he held the position of Company Head in the Home System European projects. In 1992, he joined the Department of Electrical Engineering (DEEI, now converged in the Department of Engineering and Architecture), University of Trieste, where he is currently a Deputy Director and an Associate Professor of digital communications and telecommunication networks.

Dr. Babich served as a Cochair for the Communication Theory Symposium of the IEEE International Conference on Communications (ICC) in 2005, the Wireless Communication Symposium of ICC in 2011, the Wireless Communication Symposium of the International Conference on Wireless Communications and Signal Processing in 2012, and the Communication Theory Symposium of ICC in 2014.